AN ABSTRACT OF THE THESIS OF

Jason Oak for the degree of Master of Science in Mechanical Engineering presented on July 18, 2001. Title: Flow Characteristics of Co-flowing, Laminar Streams in a Rectangular Microchannel.

Redacted for Privacy

Abstract approved: ____ _____.

Deborah V. Pence

The effects of varying flow rate ratio and Reynolds number on the momentum diffusion and flow development of two co-flowing, laminar streams in a rectangular microchannel are presented. The microchannel has an aspect ratio of approximately 16 with a width of 1006 μm and a height of 63 μm. A long, thin splitter plate initially separates the two streams such that fully developed flow in each of the two channels is obtained prior to merging. Fluorescent dye imaging and Particle Image Velocimetry (PIV) were utilized to observe the interaction between the streams for a range of flow rate ratios ranging from one to nine while maintaining a chamber Reynolds number of one. Additionally, PIV data was collected for the same flow rate ratios with a chamber Reynolds number of ten. It was found that when there is a velocity difference between the two streams, there is a cross-stream pressure gradient immediately downstream of the splitter plate that causes the faster moving fluid to expand into the slower moving fluid. Despite this rapid expansion, the fluids in two streams do not mix and continue to travel parallel to each other. As expected, the expansion of the faster moving fluid is diminished by the viscous effects present in the flow, although only at higher flow rate ratios. The merged streams eventually recover their fully developed profile although it is shown that

existing entrance length relationships do not adequately predict the development length. In addition, the velocity flow characteristics between the streams is illustrated near the end of the splitter plate. As the streams travel past the splitter plate, the flow-wise momentum of the faster moving fluid is converted into a lateral, cross-stream velocity. The presence of an optimum flow rate ratio for obtaining a maximum cross-stream velocity magnitude is suggested. The effect of varying Reynolds number on these observations is also discussed.

Flow Characteristics of Co-flowing, Laminar Streams in a Rectangular Microchannel

by

Jason Oak

A THESIS

submitted to

Oregon State University

in partial fulfillment of

the requirement for the

degree of

Master of Science

Presented July18, 2001

Commencement June 2002

Master of Science thesis of Jason Oak presented on July 18, 2001

APPROVED:

Redacted for Privacy

Major Professor, representing Mechanical Engineering

Redacted for Privacy

Head of Department of Mechanical Engineering

Redacted for Privacy

Dean of Graduate School

I understand that my thesis will become part of the permanent collection of Oregon State University libraries. My signature below authorizes release of my thesis to any reader upon request.

Redacted for Privacy

Jason Oak, Author

ACKNOWLEDGEMENT

I would like to take this opportunity to express my sincerest gratitude to Dr. James Liburdy and Dr. Deborah Pence whose support, guidance, and encouragement was invaluable in the completion of this project and my development as an engineer. I would also like to extend my thanks to the other members of my committee, Dr. Richard Peterson and Dr. Robert Leichti.

I would also like to thank all of my colleagues and friends, with special regards to Bertrand Dano and Brian Daniels, for their readiness and willingness to offer help and advice. Their assistance in the entire process did not go unappreciated.

Finally, I would like to thank my wife, Naomi, for her love, support, understanding and encouragement. I would also like to thank my parents, Kay and Chang Oak, for the love and support that they've shown me in all of my endeavors.

TABLE OF CONTENTS

TABLE OF CONTENTS (Continued)

LIST OF FIGURES

LIST OF FIGURES (Continued)

LIST OF TABLES

LIST OF APPENDIX TABLES

FLOW CHARACTERISTICS OF CO-FLOWING, LAMINAR STREAMS IN A RECTANGULAR MICROCHANNEL

CHAPTER I

INTRODUCTION

Along with the continuation of advances in microscale fabrication techniques, the number of applications for microscale fluidic devices and components is growing rapidly. Some applications include biological sensors, chemical separation devices, micro-mixers, and particle fractionation devices (Fuh, 2000). There are even some micro-fabrication techniques that utilize concepts inherent to microscale devices themselves, such as the manufacture of extremely thin fibers in capillaries and micron sized selective patterning and etching of substrates (Kenis *et al.*, 2000). With this increasing functionality, however, comes an emerging need to better understand the underlying phenomena.

One incentive for bringing applications down to the microscale level, especially those involving fluid flow, is the dramatic increase in the surface area to volume ratio. This has tremendous implications for heat transfer as well as mass transfer. The high surface area-to-volume ratio is one reason for the increasing use of the molecular separation technique known as Split-thin flow (SPLITT) fractionation. In SPLITT fractionation, two fluids containing different constituents are brought into contact in a thin, ribbon-like channel with the aid of divider plates to direct the flow. The high aspect ratio (width divided by height) of the channel allows a large amount of interfacial surface area between the fluids, and as with any transport process, this enhances the mass transfer efficiency. However, the efficacy of this technique can be greatly hampered by

turbulence. Fortunately, at small enough scales, turbulence is not existent, and diffusion, a more predictable mechanism, becomes the primary means of mixing (Brody *et al.* 1996).

The Reynolds number, Re, is a non-dimensional number that relates the ratio of the inertial to the viscous forces in a flow. The relationship describing the Reynolds number is:

$$\mathrm{Re} = \frac{\rho v l}{\mu}, \tag{1.1}$$

where ρ is the fluid density, v is the fluid velocity, μ is the kinematic viscosity, and l is the characteristic length of the device. When the characteristic length is small, the Reynolds number becomes very small, indicating that viscous forces are either comparable to, or dominate the inertial forces. Thus, when dealing with microscale fluidic devices, the small length scales keep the flow laminar even at fluid velocities that would otherwise be turbulent at larger length scales.

The present study proposes to utilize microscale visualization techniques in order to investigate the flow characteristics of co-flowing parallel streams in a microchannel. The high aspect ratio microchannel is designed such that two inlet fluid streams approach each other, initially separated by a long thin splitter plate. As the streams flow parallel along the splitter plate, it is expected that they will become fully hydrodynamically developed before they merge together in the main channel. The interaction between the two streams as they merge is the primary focus of interest. The parameters varied in this study are the velocity ratios between the two streams and the merging chamber Reynolds numbers.

CHAPTER II

LITERATURE REVIEW

This literature review describes some of the work done in the field related to the mixing and visualization of flows in microscale environments. The first section discusses some investigations into determining velocity profiles for flows in rectangular ducts. The second section deals with mixing and diffusion in microchannels. The third section discusses studies done in a particularly relevant area, SPLITT fractionation. Finally, the fourth section discusses the use of Particle Image Velocimetry (PIV) for flow visualization in small scale environments.

Velocity profiles of flows in rectangular (micro)channels

Holmes and Vermeulen (1968) utilized an early flow visualization technique to experimentally examine fluid velocity profiles in ducts of rectangular cross-section. They used rectangular ducts of four different aspect ratios (height divided by width): 1.0, 0.25, 0.15, and 0.10. Since the geometrical parameters are all given in non-dimensional variables, the actual physical dimensions of the channels are unknown. However, considering the time period in which this study was performed, it is likely the channels were not of conventional "microchannel" scales. Nonetheless, they performed this study using a phosphorescence flow visualization technique. The fluid they used in the channels was a dilute suspension of a phosphorescent powder in polybutene, a Newtonian

fluid. In order to visualize the flow, the phosphorescent suspension was exposed to a collimated light pulse from a photoflash lamp and the resulting phosphorescent trace was captured with a camera. By virtue of their optical setup, they were able to obtain a relatively thin focal plane and, thus, make measurements in the center of the channel. However, because of equipment limitations, the Reynolds number was very low such that they had "creeping" flow. Using these photographs, they were able to compare their experimental velocity profiles with the analytical solution, given as:

$$\frac{v}{v_{max}} = \frac{\sum_{k=1,3,5,\ldots}^{\infty} (-1)^{1/2(k-1)} k^{-3} \cos(\frac{1}{2} k\pi\zeta)\left\{1 - \frac{\cosh(\frac{1}{2} k\pi\xi B/H)}{\cosh(\frac{1}{2} k\pi B/H)}\right\}}{\sum_{k=1,3,5,\ldots}^{\infty} (-1)^{1/2(k-1)} k^{-3})\left\{1 - \frac{1}{\cosh(\frac{1}{2} k\pi B/H)}\right\}} \qquad (2.1)$$

where v is the velocity, v_{max} is the maximum velocity, B is the channel width (x-direction), H is the channel height (y-direction), $\xi=2x/B$, and $\zeta=2y/H$. Because of the considerable complexity involved in this solution, they also compared their data with a more simplified approximation which was derived by applying principles of minimum energy dissipation:

$$\frac{v}{v_{max}} = (1 - |\xi|^{m})(1 - |\zeta|^{2}), \qquad (2.2)$$

where the exponent m is given as:

$$m \cong 2.3 \text{ for } \frac{2}{3} \le \frac{H}{B} \le 1.0$$

and

$$m \cong 1.54\frac{B}{H} \text{ for } 0 \le \frac{H}{B} \le \frac{2}{3} \tag{2.3}$$

By plotting their data against these solutions, they found considerable agreement between their experimental results with the analytical expressions. From their experiments, it was found that for the channel of aspect ratio one, the velocity profile followed a parabolic shape as expected. However, as the aspect ratio decreased, the gradient at the wall increased, resulting in a much flatter profile that contained a more uniform velocity (v_{max}) toward the centerline of the channel.

Brody *et al.* (1996) also determined the velocity profiles in a high aspect ratio (width/height) micron scale channel at very low Reynolds numbers. The Reynolds numbers of the flow they observed were between 10^{-3} to 10^{-4}, qualifying as potential flow. Using 0.9 μm diameter fluorescent beads, they followed the flow in channels etched in silicon. The channel used was rectangular in nature, with dimensions: 11μm deep and 72 μm wide, giving an aspect ratio of approximately 67. In order to find the velocity fields, they utilized a high-speed electronic shutter on a CCD camera and recorded the elliptical streaks caused by the fluorescing beads. They determined the velocity by measuring the length of the major axis of the ellipses and the exposure time of the camera. They plotted their experimental results against that predicted by their solution to the Stokes equation given as:

$$u(x,y) = \left(\frac{Gh^2}{8\mu}\right)\frac{32}{\pi^2}\sum_{l=0}^{\infty}\frac{-1^l}{(2l+1)^3}\left\{1-\frac{\cosh(2l+1)\pi x/h}{\cosh(2l+1)\pi w/h}\right\}\cos[(2l+1)\pi y/h] \tag{2.4}$$

where G is the pressure gradient, μ is the viscosity, w is the width of the channel (x-direction), and h is the height of the channel (y-direction). Given that they did not attempt to resolve the depth-wise positions of the particles in the channel, they found "excellent agreement" between their experimental data and the analytical solution.

In a more recent study, Gosch *et al.* (2000), studied the velocity distribution in a square shaped duct. They used a confocal epi-illuminated microscope in order to perform fluorescence correlation spectroscopy at the central plane of a 50 μm by 50 μm microchannel etched into a silicon oxide wafer. In order to allow visualization of the flow, the open side of the channel consisted of an etched glass wafer that had been anodically bonded to the silicon. The flow was "seeded" with a dilute concentration of fluorescent molecules (TMR-4-dUTP in water). Using an auto correlation function determined from the fluorescence intensity fluctuation, they were able to determine the velocity profile in the flow at a very high spatial resolution of 0.4 μm. By varying the pressure head (ΔP) driving their flow and measuring the resulting velocity (v), they found that the linear relationship as defined by the Hagen-Poiseuille equation,

$$v(x) = \frac{\Delta P}{2\eta l}(d^2 - x^2), \tag{2.5}$$

was satisfied by the flow in the microchannel, where l is the length of the channel, d is half the width of the channel, and x is the flow-wise position of the channel. By plotting the velocity measurements across the microchannel with an aspect ratio of one, they also found the expected parabolic velocity profiles across the centerline of the channel in both dimensions.

Diffusion and mixing in microchannels

Kenis *et al.* (1999) used the laminar flow properties inherent in small capillaries and microchannels to develop a novel micro-fabrication process. They utilized the observation that at low Reynolds numbers, multiple distinct streams flowing in parallel in a capillary do not develop turbulence and the only manner in which mixing can occur is through diffusion across the interface of the fluids. By introducing various chemical reactants into a 200-μm wide channel, they were able to demonstrate spatially selective etching of capillaries as well as the fabrication of thin wires inside capillaries. They also demonstrated that the streams were able to maintain parallel, non-mixing, laminar flow through bends greater than 90 degrees for long distances on the order of several centimeters. They also note that the laminar nature of the flow allows the location of the liquid-liquid interface in a fluidic device to be finely positioned by controlling the relative volumes of the incoming streams.

In addition to velocity profile measurements, Brody *et al.* (1996) also describe another experiment in which they demonstrate a "low Reynolds number filter" useful for liquid-liquid extraction. The flow device used was an H-shaped channel, with two inlets and two outlets. One of the inlet streams contained a mixture of green fluorescent dye (Fluorescein) and 0.2-μm red fluorescing microspheres, while the other contained buffer. The two initially separate laminar flow streams approach each other at 180 degrees but as a result of the laminar nature of the flow, they do not mix, and merely follow the 90 degree bend. The two streams then flow parallel in a larger chamber, where diffusion

across the boundary can occur. At the end of the channel, the flow splits in a manner similar to which it merged. Using the fluorescent properties of the dye and the microspheres, they were able to show that the dye, with its larger diffusion coefficient (D=500 $\mu m^2/s$) was able to diffuse from the carrier stream to the other stream. Conversely, the fluorescent microspheres, with their lower diffusion coefficient (D=1 $\mu m^2/s$), did not diffuse into the other stream. Therefore, by manipulating the flow parameters, they were able to validate an efficient method of using the non-mixing properties of laminar flow in microchannels.

Ismagilov *et al.* (2000) studied the convective and diffusive transport processes occurring in a high aspect ratio, Y-shaped, microchannel at low Reynolds numbers and high Peclet numbers. Using confocal fluorescent microscopy, they were able to visualize the three-dimensional structure of a chemical reaction occurring at the interface of two reactants as they flowed down the channel. The height of the channel (the short dimension) was 60 μm. They noted that the high aspect ratio results in a higher fraction of slower moving fluid near the walls across the short dimension of the channel. As a result of the slower velocity, there is more cross-stream diffusion near the walls of the channel since the contact time between the two streams is increased. Thus, they found that the degree of diffusive mixing scales as the one-third power of the downstream axial distance near the walls, while it scales as the one-half power of the axial distance at the center of the channel. They also ascertained that near the walls, mixing between the streams scales inversely with the one-third power of the maximum fluid velocity,

whereas near the centerline, it scales inversely as the one-half power of the average velocity.

Flow analysis of SPLITT fractionation microchannels

One application of high aspect ratio microchannels is Split-flow thin (SPLITT) fractionation. SPLITT fractionation is of particular interest because of the geometric similarities to the current experimental device under investigation. SPLITT fractionation is a separation technique used to separate particles and other macromolecules in a fluid flow. SPLITT channels are usually very thin, "ribbon-like" channels (< 500 μm) with a splitter plate at the inlet and the outlet (Fuh, 2000). Usually, two inlet flows are used: the "feeder" stream, which carries the particles to be separated, and the "carrier" stream, which is normally a buffer solution. A thin splitter plate initially separates these flows, after which they merge and the separation process begins. A driving force, usually gravitational, centrifugal, electrical or magnetic is applied perpendicular to the flow direction to facilitate the separation process. (Fuh, 2000). This driving force, coupled with diffusion between the two streams, causes the particles to move from the feeder stream into the carrier stream. By controlling the flow ratios between the feeder and carrier streams, the location of the interface between the two can be adjusted such that a second splitter plate near the exit of the channel can separate and divide the two resulting flows. Unlike in the current study, the splitter plates in SPLITT channels are aligned

such that the separation occurs across the short dimension of the channel. However, the interaction of the streams as they flow past the splitter plate in the flow is still of interest.

Using both experimental and numerical analysis, Fuh *et al.* (1995) studied the hydrodynamic effects in a 0.0381 cm x 4 cm x 20 cm SPLITT channel. One of the fundamental requirements for effective particle separation in SPLITT channels is that there is no mixing between the streams, since this would reduce the efficacy of the applied transverse separation force (Fuh, 2000). In order to observe this, they injected a dye into one of the streams to observe the stream paths. Unfortunately, due to experimental anomalies, the results of this test were not definitive. They also used a computational fluid dynamics software package, FLUENT, to solve the two-dimensional Navier-Stokes equations (isothermal flow and constant properties) to find information about the flow around an inlet splitter plate with a thickness equal to one-third of the channel width. Using Reynolds numbers of 0.42 and 42 with an inlet flow ratio of four, they found that disturbances in the flow resulting from the splitter plate tend to vanish after a few channel thicknesses downstream. However, when the flow ratio was increased to 13 (Reynolds number = 20), they observed the formation of a vortex in the slower stream. Furthermore, by altering the geometry of the splitter plate from a blunt end to a stepped end, they found that the vortex formation was reduced for similar flow conditions.

In another study, Ligrani *et al.* (1998) examined, both experimentally and numerically, the mixing that develops in the shear layer between two co-flowing streams flowing with different velocities and densities. While most research on this topic has

been focused in the area of geophysical flows with shear-induced mixing, they examined these mixing effects at the much smaller scales associated with SPLITT fractionation. For the flows involved in this study, they used Reynolds numbers from 1.1 to 5.6 and absolute values of Richardson numbers (ratio of the square of the natural to the forced convection velocity scales) ranging from 10^{-3} to $2x10^{-1}$. However, because of the way in which they defined these non-dimensional numbers, they are not directly comparable to others mentioned in this review. They used a commercial CFD software package, FLUENT in order to solve the Navier-Stokes equation governing the flow. Because of the high aspect ratio, they assumed that the flow was two-dimensional in their computations. They generated plots of the velocity profiles at various points, before and after the splitter plate, to generate a characteristic length used for the non-dimensional numbers. Nonetheless, the resulting velocity profile plot illustrates the diffusion of momentum from the faster moving stream to the slower moving stream as the flow progresses downstream beyond the splitter plate. The experimental channel used was 635 μm thick, and 4 cm wide resulting in a high aspect ratio of 63. The inlet splitter plate used was 127 μm thick and sufficiently long enough to assume fully developed flow at the end. The fluid used was an aqueous solution of FL-70 detergent and sodium azide bactericide. A sucrose solution was selectively added to one or the other stream in order to create the desired density stratification stability. Polystyrene latex particles with diameters ranging from 1 to 35 μm were mixed with one of the streams. The particles essentially acted as tracers that indicated the amount of mixing and entrainment between the two fluid streams in the channel. Utilizing the size and spatial distribution of particles

in either of the two outlets channels, they developed a "mixing onset parameter," R, which gives an indication of the amount of mixing and entrainment occurring in the channel. Essentially, the more uniform the particle distribution in the separated exit flow, the more mixing that occurred in the channel. By varying the Richardson and Reynolds numbers, they found that mixing due to flow instabilities was a stronger function of the Richardson number. This indicates that shear gradients resulting from high velocity ratios tend to play a smaller role in mixing than density gradients.

Particle Image Velocimetry (PIV) studies in microscale environments

With advances in microscale manufacturing techniques, there has been increasing interest in being able to acquire localized flow information within these microscale environments. However, because of the small size of the channels, the insertion and utilization of probes for obtaining velocity measurements is precluded. Therefore, a non-invasive method such as PIV is more suitable for obtaining flow characterization. The fundamental premise for PIV is relatively simple. Using a tracer in the fluid, multiple "snapshots" of the fluid and the position of the tracers in the fluid are obtained with a known time separation. By measuring the displacement and knowing the time separation, the velocity can be determined. Through the use of many tracers in the fluid, a velocity vector field can be obtained. While there are many similarities between microscale PIV and macroscale PIV, there are some additional complications involved with the former, such as difficulties in gaining optical access to the flow for visualization, diffraction

effects, and obtaining adequate intensity signals from micron sized particles (Wereley *et al.*, 1998). Nonetheless, there have been a number of studies that have utilized various PIV techniques to provide more details of microscale flows.

Santiago *et al.* (1998) describe an epi-fluorescence-based micro-PIV system developed in order to obtain micron resolution vector field images of flow in microscale fluidic devices. They utilized this system with 100 to 300 nm diameter fluorescent polystyrene spheres to observe the Hele-Shaw flow around a 30-μm elliptical cylinder. Using high magnification optics, they were able to obtain a velocity field with a vector spacing of 3.45 μm over a 120 μm x 120 μm field of view. In a later study, Wereley *et al.* (1998) applied this imaging system to observe a Hele-Shaw flow around an 8-μm diameter red blood cell. They were able to obtain a velocity field with a vector spacing of 3.2 μm over a 30 μm x 30 μm area. However, in both of these studies, the time between successive image pairs was on the order of milliseconds, limiting them to very slow flows with Reynolds numbers on the order of 10^{-3}. In a more recent study, Meinhart *et al.* (1999) modified the micro-PIV system to include two Nd:YAG lasers as the light source. This enabled them to decrease the time separation between images, allowing the analysis of faster flows. They used this modified system along with a customized cross-correlation algorithm to study flow in a 30 μm x 300 μm x 25 mm rectangular channel. Using this PIV system, with a focal plane resolution of approximately 1.8 μm, they were able to obtain near-wall velocity profiles and demonstrate that they match up well with the analytical solution for flow through a rectangular channel.

In another approach, Cummings (1999) developed a micro-PIV system in which the depth-wise resolution of the flow under observation is not controlled by the optical setup, but rather by a software processing algorithm. The effectiveness of this technique was demonstrated on an electroosmotically driven flow at low Reynolds numbers through an array of 30-μm tall cylindrical posts. However, the authors note that this technique is limited to low Reynolds numbers in which the depth-wise velocity gradients are small.

CHAPTER III

EXPERIMENTAL SETUP

This section discusses the overall design of the experiment and gives details on the instrumentation used for data acquisition. The experimental setup used for the fluorescent dye portion of the study was slightly different from the one used for the PIV portion of the study. Schematic overviews of the different experimental setups are shown in Figure 3.1 and Figure 3.2 for the fluorescent dye study and PIV study, respectively. Despite their differences, both contain the same basic components. These include the microchannel, the microchannel fixture system, the flow loop, and the optical setup. They are discussed in the following sections.

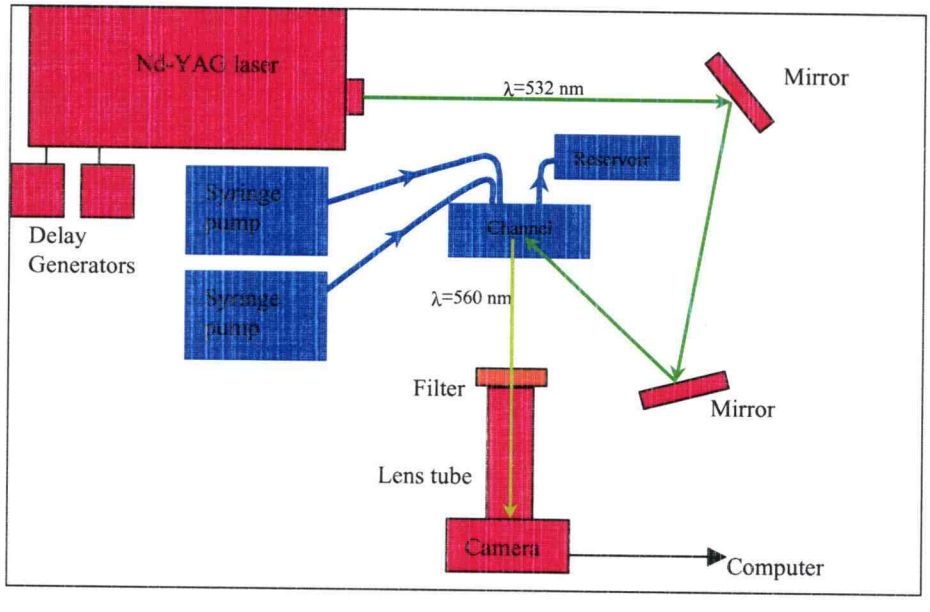

Figure 3.1
Schematic overview of fluorescent dye setup. The flow loop is indicated in blue while the optical components are in red.

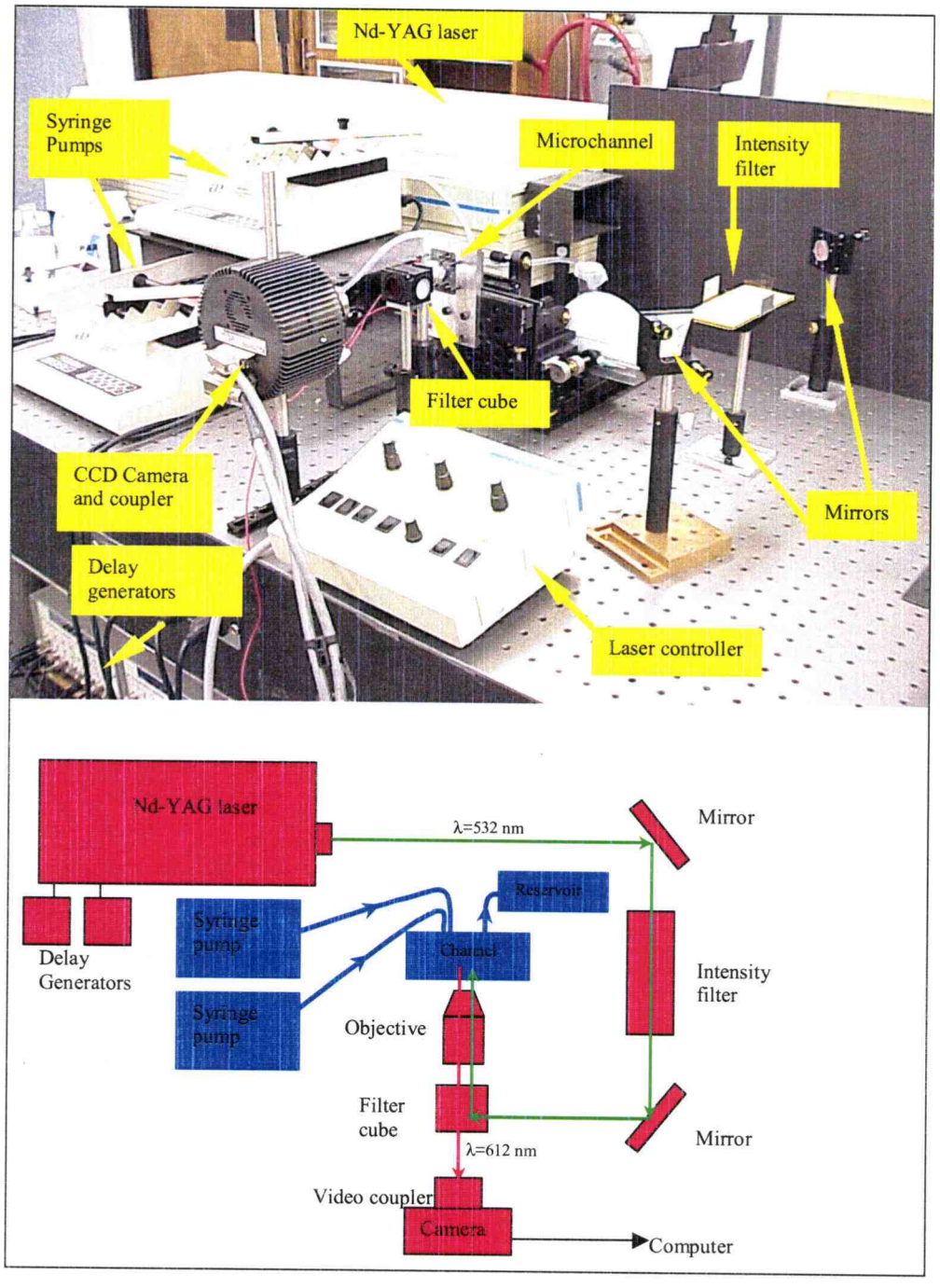

Figure 3.2
Schematic and actual overview of PIV setup. (a) The actual setup, (b) Schematic view. The flow loop is indicated in blue while the optical components are in red.

Microchannel construction

Laminate construction was used to design and build the microchannel flow device. This manufacturing technique was chosen due to the relatively low manufacturing costs and the availability of resources. The device consisted of seven layers: a single layer of stainless steel, two layers of glass, an aluminum spacer, a polycarbonate layer, and a pair of carbon steel collars (Figure 3.3). The innermost stainless steel layer, 50.8 μm thick, formed the walls of the flow channel (Figure 3.4). The overall layer dimensions were 25.1 by 33 millimeters. Using an ESI 4410 Nd-YAG laser, frequency doubled into the UV range (1064 nm), the channel was laser machined out of the steel layer in the shape of a "Y", such that the top of the "Y" formed the two inlets and the bottom end of the "Y" formed the single outlet. The two inlet channels approach each other at a 90-degree angle and then are directed such that they flow parallel to each other. They are initially separated by a thin splitter plate, 3.5 mm long and approximately 91 μm wide. After the end of the splitter plate, the two streams are free to contact and interact with each other for approximately another 3.5 mm before the channel flow reaches the exit. Due to the machining process and the flexibility of the splitter plate, the inlet channels were not exactly equal in cross-sectional flow area. Using a calibrated video microscope, the top channel was measured to be 472 ± 2 μm wide and the bottom channel was 443 ± 2 μm wide, a difference of approximately 6%. The total width of the channel was 1006 ± 2 μm, varying only 2 μm over a 7 mm length.

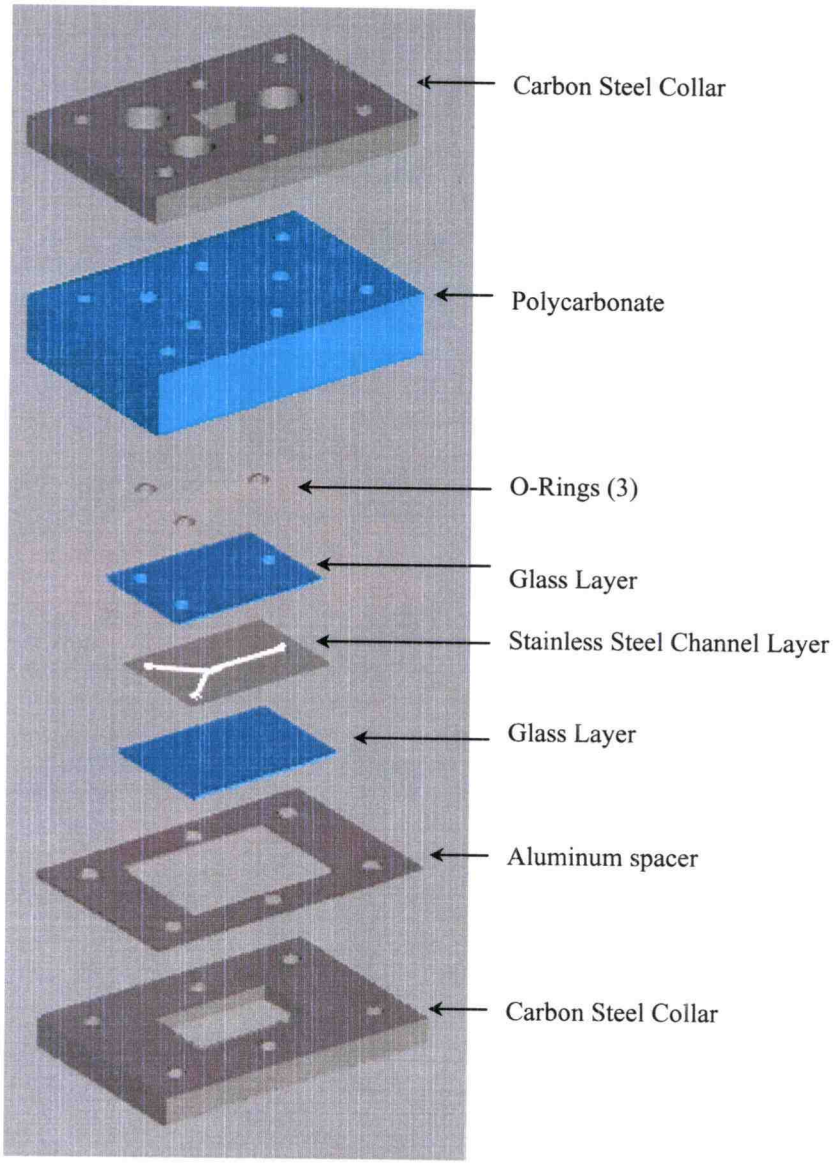

Figure 3.3
Exploded view of microchannel device

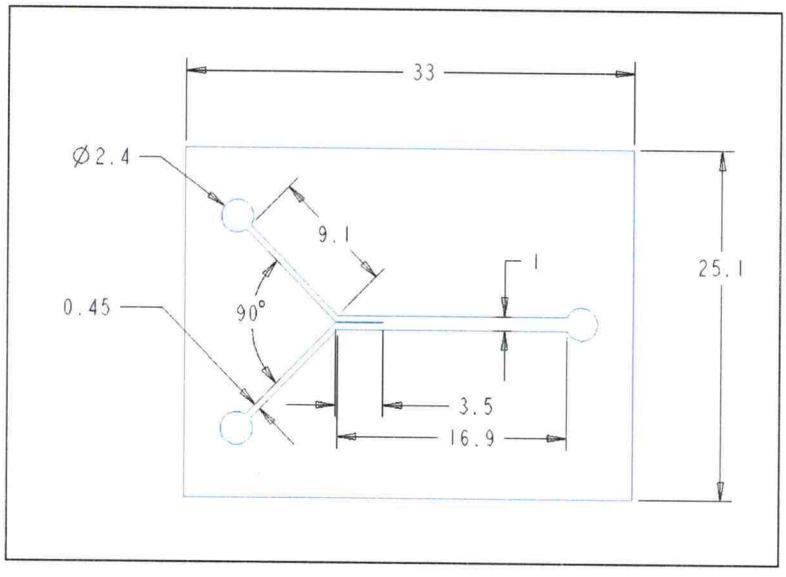

Figure 3.4
Detailed view of stainless steel channel layer geometry. Dimensions are in mm.

On either side of the steel channel layer were two cut pieces of Fisher Scientific glass microscope slides, approximately 1 mm thick with the same overall dimensions as the channel layer. These formed the other two walls (top and bottom) of the rectangular microchannel. Glass was chosen because of its relative smoothness and also to allow a transparent path through which to perform visualization. However, because of the relative roughness of the laser cut stainless steel, a thin layer of vacuum grease was applied between the glass and stainless steel to fill any gaps. Great care was taken to apply the grease such that it would not seep into the channel. Through one of the glass surfaces, three holes were drilled to allow a throughway for the two inlets and single outlet.

This drilled glass piece was embedded in a polycarbonate layer which had three matching flow channels drilled though. Three o-rings were placed at the interface between the glass and the polycarbonate to form a seal. The polycarbonate was 17.8

millimeters thick and 43.2 by 61 millimeters in area. The polycarbonate layer was necessary because of the difficulties involved in adequately machining glass to accept the necessary fittings. On the opposite side of the polycarbonate, three $1/16^{th}$ inch ID threaded polyethylene fittings were connected to allow a connection between the device and the rest of the flow loop.

Surrounding the other, undrilled, glass layer was an aluminum spacer that was sanded down such that it was slightly thinner than the combined glass and stainless steel layer thickness. The purpose of this layer was to add structural support such that when pressure was applied to the device, it would not become unstable and crack the glass.

On the outside of the device was a carbon steel collar. One of the layers contained holes for the fittings and flow path to pass through while the other contained a beveled "viewing window" to allow for visualization. Six 1.5-inch alloy steel bolts were passed through all the layers (excluding the glass and channel layers) to clamp the device and seal it together. The steel collar also helped to distribute the clamping force close to the channel walls. The bolts were evenly tightened to approximately 15 in-lbs as measured by a Proto 6169A dial torque wrench. After the device was assembled, the depth of the channel was measured using a Leica TCR inverted microscope by focusing on the top and bottom planes of the channel. The overall depth was found to be 63 ± 3 μm. The assembled device is shown in Figure 3.5

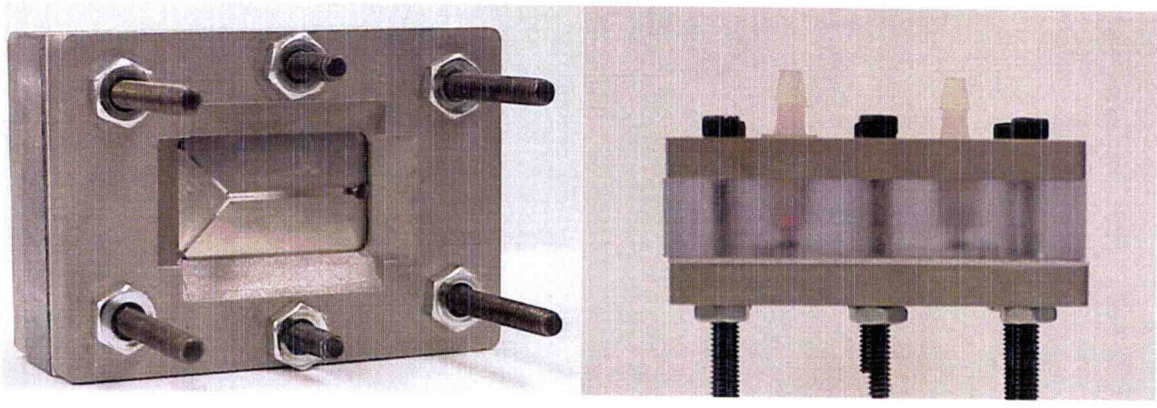

Figure 3.5
Pictures of assembled microchannel device. Left: Visualization side. Right: Side view.

Mounting fixture

Because of the relatively small length scales involved and the desire to gather information near the center of the channel, alignment of the channel was critical. In addition, since the optical system was a fixed system, focusing was achieved by adjusting the relative position of the channel. At the micron scale level, this is not a trivial feat. This matter was addressed by configuring a fixture device that could be adjusted in six degrees of freedom. This gave precise control over the orientation of the channel relative to the imaging acquisition system. The actual alignment of the channel was performed by focusing in on small reference marks scratched into the four corners of the glass layer. Once a mark was placed into focus, the channel was moved either transversely or longitudinally until the next reference mark was in view. If no additional focusing adjustments were necessary, the channel was considered aligned. This was repeated until all four reference marks were aligned with the focal plane of the optical system.

In order to gather data at the center of the microchannel, it was necessary to be able to place the focal plane at the center. However, the lack of any features to focus on in the center of the channel made it impossible to place the focal plane in the center of the channel. Instead, focal plane placement was done by focusing on the front side of the steel channel layer and then moving the channel forward approximately 31 μm, or half the actual thickness of the channel. The use of an 80-pitch actuator (80 turns per inch of lateral movement) enabled relatively accurate movement of the channel in and out of the focal plane. Therefore, in order to move 31 μm,

$$(31\mu m)\left(\frac{1cm}{10000\mu m}\right)\left(\frac{1inch}{2.54cm}\right)\left(\frac{80turns}{1inch}\right)\left(\frac{360degrees}{1turn}\right)=34.0degrees$$

the micro-actuator was turned 34 degrees.

Flow loop

The flow loop is shown in blue in Figure 3.1 and Figure 3.2. Two internally calibrated Cole-Parmer 74900-Series Multichannel Syringe Pumps independently controlled the flow rates into the two inlets of the device. The accuracy of the pump as given by the manufacturer is ±0.5% and the reproducibility is ±0.2%. Hamilton GasTight 10-ml glass syringes were used in each of the pumps. The syringes were connected to the microchannel device fittings with $1/8^{th}$ inch inner diameter Tygon tubing. The device outlet was then connected to another length of Tygon tubing and collected into a reservoir.

Optical/Visualization setup:

This is where the experimental systems for the two flow imaging experiments diverge. The PIV optical setup will be discussed first.

PIV setup

The optical components are the ones shown in red in Figure 3.2. The main components of the system include a pulsed, dual head, dual Q-Switch, Spectra Physics PIV-400 Nd:YAG laser with two Stanford Research Systems DG535 digital delay generators, a series of glass coverslips to reduce the beam intensity, an epi-fluorescent cube, a 10X Plan Apochromat lens, a 0.5X video coupler, a Princeton Instruments, Inc. MicroMAX 5-MHZ cooled CCD camera, and a Pentium II 350-MHz Gateway PC for image acquisition.

The Q-switched dual head Nd:YAG laser is capable of firing two high intensity pulses of 532-nm wavelength (green) light within 2 μs at a rate of 15 Hz. The synchronization and time separation between each pair of pulses was controlled by a pair of delay generators.

When operating at full power, the Nd:YAG laser outputs a very high amount of energy, sufficient to damage the channel. However, when run at a lower setting, the quality of the light beam begins to deteriorate. In order to circumvent this problem, a "beam intensity filter" was used. The filter consisted of 6 glass coverslips aligned at a 45-degree angle to beam path. Approximately 8% of the light is reflected away each time the beam passes through a coverslip, reducing the intensity of the beam. This enabled the Nd:YAG laser to be run at full power without damaging the microchannel.

A Nikon Wide Green Excitation G-2A epi-fluorescent filter cube lies at the heart of the optical system. The cube contains three elements: an excitation filter, a dichroic mirror, and an emission filter (Figure 3.6). The excitation filter serves to pass only light with wavelengths between 510 and 560 nm. This filtered light then reflects off the dichroic mirror (or beamsplitter) toward the subject to be illuminated. Of the light that comes back from the subject, only light with a wavelength outside the excitation wavelengths (510 to 560 nm) is allowed to pass through the dichroic mirror. Finally, the emission filter allows only wavelengths above 590 nm to pass through to the CCD camera. The transmission spectra for the various components of the cube are shown in Figure 3.7

A Nikon 10X Plan Apochromat microscope objective lens was chosen because of its high numerical aperture, low distortion and correction characteristics for spherical and chromatic aberrations. The 0.5X C-mounted video coupler was necessary in order to achieve a low enough overall magnification (5X) to view the entire channel width in a single frame, but still maintain a relatively high numerical aperture (0.3)

The camera used was a Princeton Instruments, Inc. MicroMAX 5-MHZ camera with a CCD array resolution of 1300 x 1030 pixels. The camera utilized a cooled array which enables a better signal to noise ratio. The timing and synchronization of the camera with the laser was controlled by the delay generators.

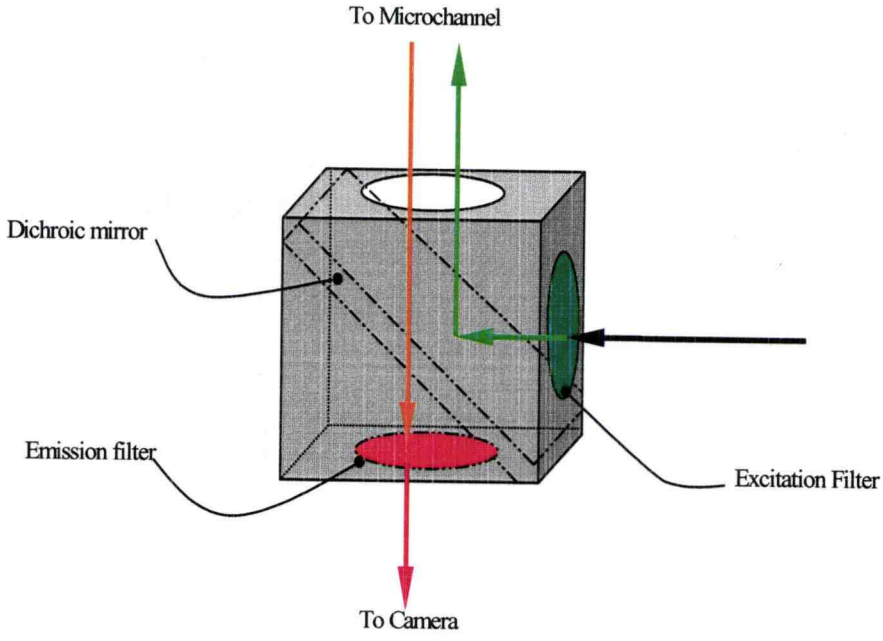

Figure 3.6
Schematic of dichroic mirror

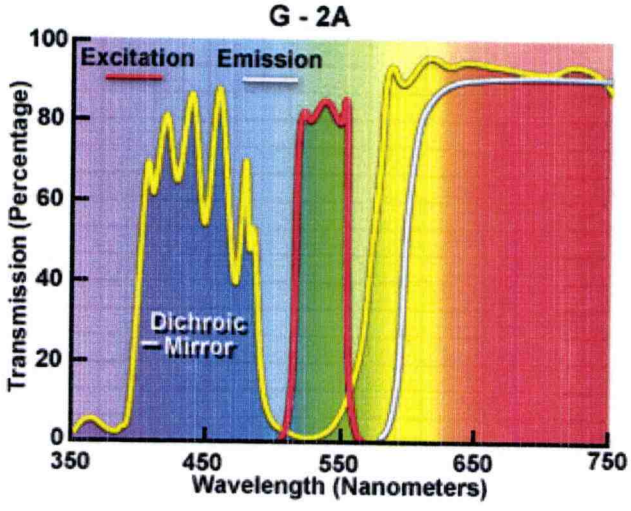

Figure 3.7
Transmission spectrum for Nikon G-2A epi-fluorescent cube. Used with permission from the Nikon MicroscopyU web page.

According to Meinhart *et al.* (1999), in order to estimate the total depth of field (δz), considering diffraction as well as geometric effects, equation 3.1 can be used:

$$\delta z = \frac{n\lambda}{NA^2} + \frac{ne}{M \cdot NA} \tag{3.1}$$

where n is the index of refraction of the medium between the device and the objective, NA is the numerical aperture, M is the total magnification of the system, λ is the wavelength of the emitted light, and e is the pixel spacing of the CCD array. In this case, the medium is air, so n=1.003 and the pixel spacing of the CCD is 6.7 μm as given in the manufacturer specifications. Therefore, the depth of field is estimated to be approximately 11 μm.

Fluorescent dye setup

Because of incompatible specifications, a simple optical filter was used for the dye study instead of an epi-fluorescent cube. The filter removed the unwanted scattered light and allowed only the light from the fluorescence of the dye to transmit through. As a result, instead of lighting up the channel through the camera optics, the channel had to be illuminated at an angle. The filter was chosen to selectively let light of wavelengths centering around 560 nm to pass through. Additionally, the lens system for the camera was changed to an Infinity Photo Optical C. Model KV far microscope lens and Infinity Photo Optical Co. DL Tube lens doublers.

Flow additives

For the PIV studies, the flow was seeded with 2.0-μm diameter fluorescent dyed polystyrene beads (Duke Scientific, catalog number R0200). The beads came packaged in a solution of approximately 2.4 x 10^9 beads per ml of solution. This was then diluted with deionized water at a ratio of 1 to 30. As stated in the manufacturer literature, the microspheres have a density of 1.05 g/ml. The excitation maximum is at 532 nm, which corresponds to the wavelength of the Nd:YAG laser. The emission maximum is at 612 nm (red), which is compatible with the high pass emission filter in the epi-fluorescent filter cube.

A 10^{-3} molar solution of Rhodamine 6G Chloride (Molecular Probes, R-634) in water was used in the fluorescent dye study. The fluid in the other stream was deionized water. The fluid properties of the Rhodamine 6G solution were assumed to be identical to those of water. The binary diffusion coefficient for Rhodamine 6G was given to be $D=2.8x10^{-10}$ m^2/s. The dye has maximum excitation at a wavelength of 525 nm, and a maximum emission at 560 nm. Both of these are within the proper specifications of the optical system.

CHAPTER IV

PROCEDURE AND DATA REDUCTION

This section discusses the details of the procedure used to obtain and process the data for the fluorescent dye study and the PIV studies.

Fluorescent dye study

For either of the studies, it was extremely important to make sure there were no bubbles in the flow system or the channel. Once the 10^{-3} molar Rhodamine 6G chloride dye and deionized water had been successfully loaded and attached to the channel, the channel was adjusted so that the focal plane was within the channel. Then, in order to achieve the desired flow/velocity ratios, the following flow rates were input into the syringe pumps:

Table 4.1 Flow conditions for fluorescent dye study.

	Reynolds number = 1	
Flow ratio	**Flow rate (μl/min) (slow stream)**	**Flow rate (μl/min) (fast stream)**
1:1	15.83	15.83
1:3	7.893	23.68
1:5	5.263	26.31
1:7	3.947	27.63
1:9	3.158	28.42

Unfortunately, due to equipment failure, the Reynolds number ten case could not be run. The flow rates were chosen such that the main channel Reynolds number remained constant at one. The Reynolds number was based on the hydraulic diameter,

$$d_h = \frac{4WH}{2(W+H)}, \tag{4.1}$$

where H is the height of the channel (63 μm) and W is the width of the channel (1006 μm). The viscosity and density were taken to be that for water at atmospheric conditions.

Once the flow had stabilized for each velocity ratio (approximately 1-2 minutes), an image of the flow near the splitter plate was taken. This image was then saved in TIFF format and run through various Matlab (version 5.3) filters to process and clean up the images.

PIV study

For the PIV study, a solution of 1-part polystyrene bead solution to 30-parts deionized water was prepared. Once the solution was loaded into both syringes, the channel and optics system was aligned. The following table gives the flow rates used to achieve the desired flow ratios:

Table 4.2 Flow conditions for PIV study.

	Reynolds number = 1		**Reynolds number = 10**	
Flow ratio	**Flow rate (μl/min) (slow stream)**	**Flow rate (μl/min) (fast stream)**	**Fast stream (μl/min) (slow stream)**	**Slow stream (μl/min) (fast stream)**
1:1	15.83	15.83	158.3	158.3
1:3	7.893	23.68	78.93	236.8
1:5	5.263	26.31	52.63	263.1
1:7	3.947	27.63	39.47	276.3
1:9	3.158	28.42	31.58	284.2

PIV measurements were obtained in order to generate velocity vector fields of the region around the splitter plate. For each Reynolds number and velocity ratio, several pairs of images were taken. The timing was fixed such that for a Reynolds number of one, the time between each pair of images was 400 μs. The camera exposure time was set accordingly at 300 μs (Figure 4.1). Similarly, for a Reynolds number of ten, the time between each image was 40 μs and the camera exposure time was reduced to 200 μs (Figure 4.2). This timing was chosen to give an average particle displacement of 4 pixels between each image. Each pair was saved as a double-framed SPE file by the WinView32 software acquisition program. These files were then split into single framed 8-bit TIFF files to be analyzed using Visiflow (ver. 6.11) PIV analysis software.

Velocity vector fields were obtained from each pair of split files using a cross-correlation method. Each pair was evaluated using a 64 x 64-pixel interrogation window with 75% overlap between the regions. This resulted in a 56 x 69, two-dimensional vector field. Subtracting the vector region occupied by the splitter plate (156 vectors) resulted in a vector field with 3708 vectors. The vector field covered an area of approximately 1008 μm by 1242 μm, resulting in a vector spacing of 18 μm. A boundary mask was first applied to the files to indicate where the walls of the channel and the splitter plate were located. A velocity of zero was specified in these regions. Once each PIV image pair was analyzed by the software, the flow field was inspected for any spurious vectors. These are individual vectors that were not within the normal flow parameters (i.e. if the magnitude or directions were grossly inconsistent with the surrounding flow field). If they were found, then the "next best vector" feature of Visiflow was used to find a vector that was more congruent with the surrounding flow.

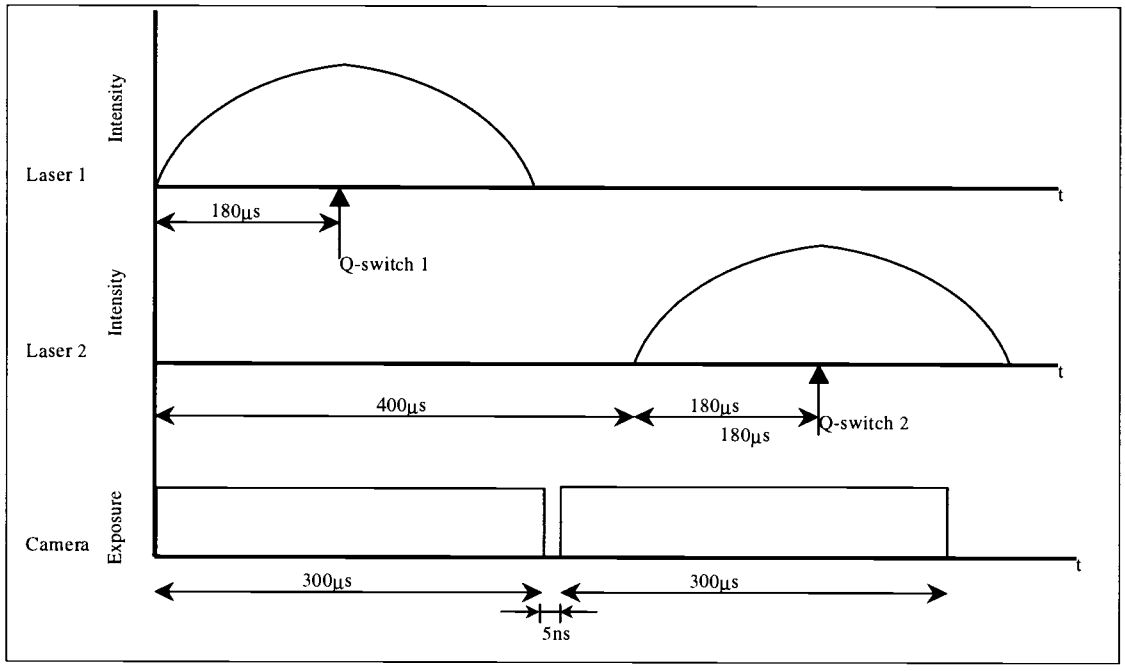

Figure 4.1
PIV Timing diagram for Reynolds = 1. Time between laser pulses = 400 μs, Exposure time per image= 300 μs.

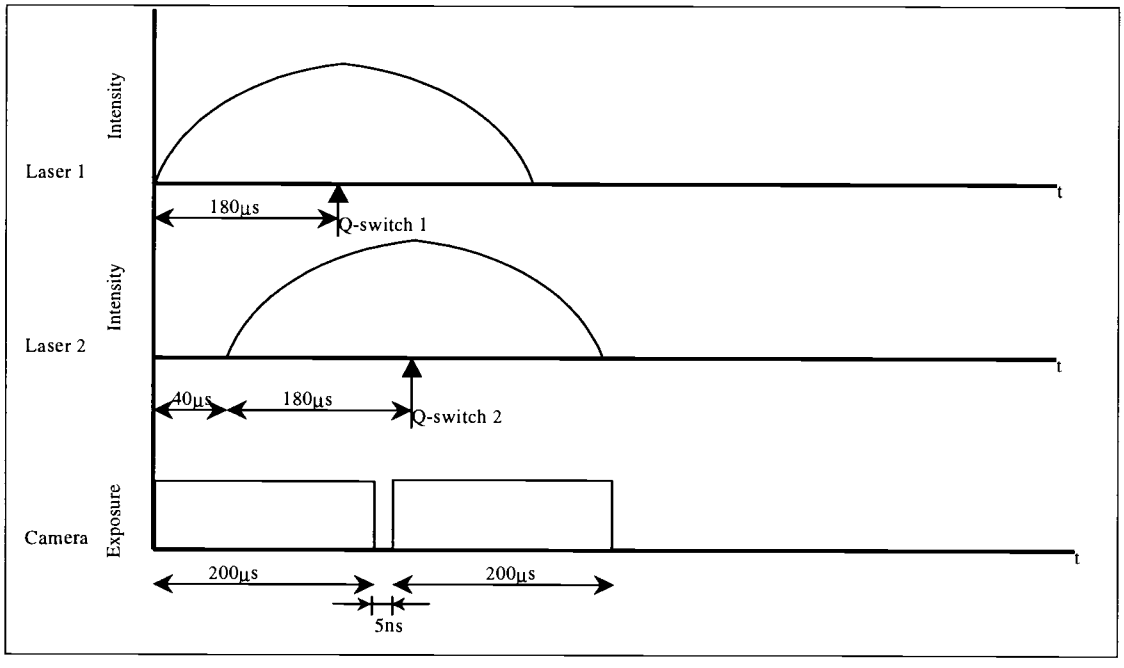

Figure 4.2
PIV timing diagram for Reynolds = 10. Time between laser pulses = 40 μs, Exposure time per image = 200 μs.

On average, this was only engaged for 10-20 vectors per image, representing less than 1% of the total flow field. This was done in hopes of preventing further propagation of erroneous results. Once the analysis was done, the velocity vector field data (position, magnitude, and direction) were exported to an ASCII file. This file was then imported into Matlab for further analysis. Among the various Matlab functions, the "quiver" function was used to obtain vector plots of the total velocity, the stream-wise component of velocity, and the cross-stream component of velocity. Additionally, the "pcolor" function was used to generate color contour plots of the velocities as well.

CHAPTER V

RESULTS AND DISCUSSION

This section describes and discusses the results obtained in this study. The results are divided into two main sections: (i.) observations from the fluorescent dye study, and (ii.) the PIV results.

Fluorescent dye results

In this part of the study, a solution of 10^{-3} molar Rhodamine 6G Chloride dye was used to visualize the flow in the microchannel. By using the dye in one channel inlet and deionized water in the other, the two fluid streams flowing in the microchannel could be differentiated. As they flowed past the splitter plate and merged together, the fluorescence of the dye stream enabled the observation of the interaction between them as they continued downstream. Two images of the entire parallel section of the flow channel, including the length of the splitter plate, are shown in Figure 5.1. The top image shows the condition where the flow ratio between the two channels is one-to-one for a Reynolds number of one. The most noticeable aspect of this image is the lack of mixing and interaction between the two streams. In this case, the flow from the top (dye) and bottom (water) merely flow around the splitter plate and meet at approximately the middle of the channel. Since the intensity of the fluorescence is proportional to the concentration of dye in the fluid, gray regions would indicate the presence of mixing. Apparently, there is very little observed mixing occurring. Additionally, as the flow

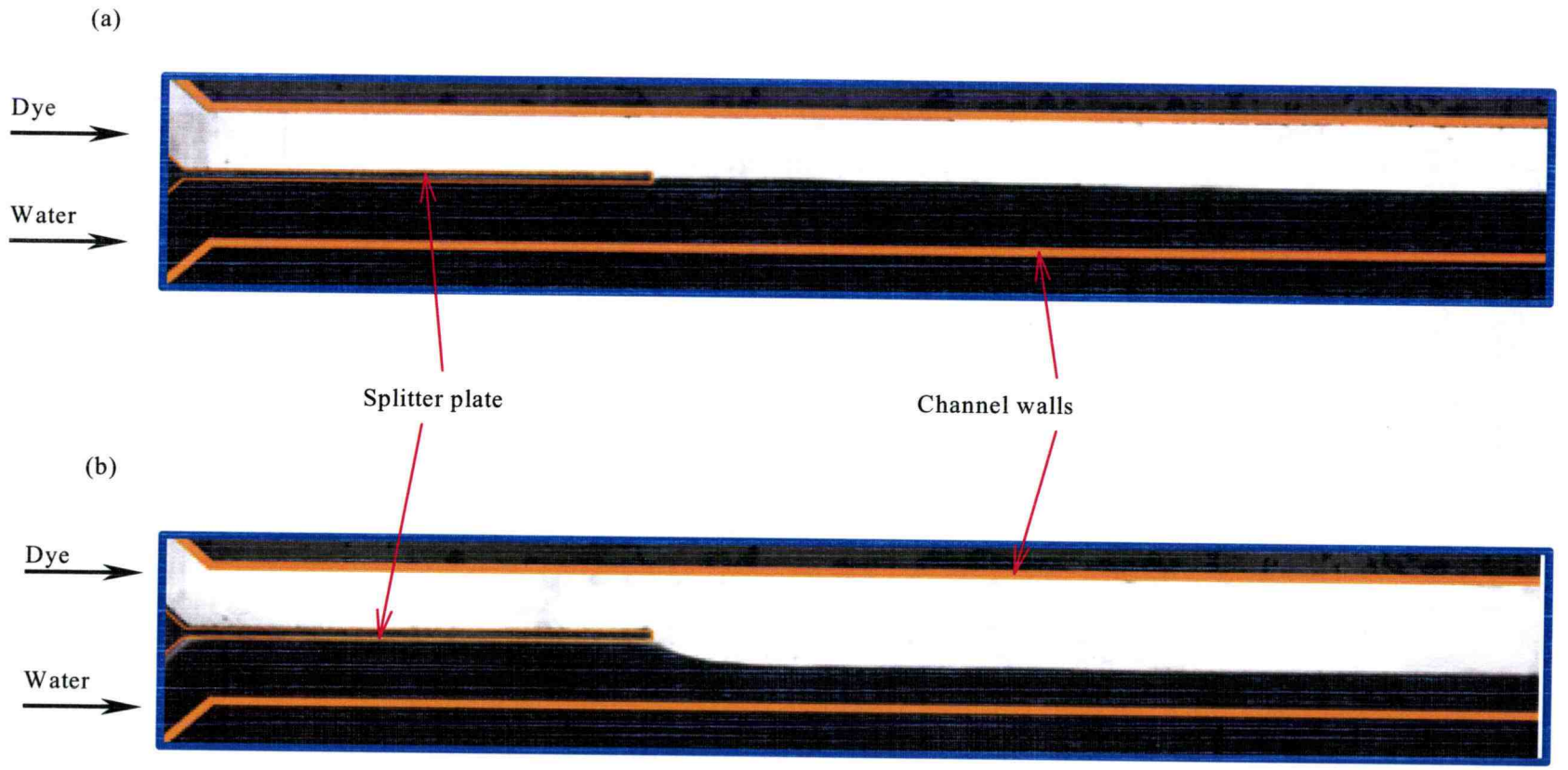

Figure 5.1
Fluorescent dye images of full length of microchannel. The flow is from left to right. The white region is the fluorescent dye. The orange lines indicate the boundaries of the channel. (a) Flow ratio is one-to-one; (b) Flow ratio is one-to-three

progresses downstream, there is no observable diffusional expansion of the dye into the water stream.

In the bottom image of Figure 5.1, the flow ratio of the two channels is one-to-three. In this situation, once the streams pass the end of the splitter plate, the faster moving dye stream (shown as white in the image) is shown to expand into the slower water stream (black). This is a result of the momentum of the faster moving fluid expanding into the slower moving fluid. Once the lateral momentum transfer diminishes, the dye and water streams continue in a parallel fashion down the remainder of the channel. Even though there is a velocity difference between the two streams and a resulting high velocity gradient and shear stress at the interface, no noticeable mixing occurs. This same pattern of behavior was also observed for all subsequent velocity ratios. The major difference was with the extent to which the faster stream expanded into the slower one, which increased for larger flow ratios. The lack of cross-stream diffusion as the fluid travel down the channel is in agreement with the results discussed earlier in which Kenis *et al.* (1999) found no diffusional broadening over several centimeters in capillary fluid flow. However, in that case, they used much higher flow rates than the ones imposed here in an attempt to suppress the diffusion between the fluids along the length of the channel. Since some degree of cross-stream diffusion would be expected in this experiment, given the flow parameters, one explanation for its absence could be the relatively low diffusion coefficient, $D=2.8\times10^{-10}$ m^2/s, for Rhodamine 6G Chloride.

The images in Figure 5.2, Figure 5.3, and Figure 5.4 focus on the regions near and just downstream of the end of the splitter plate. Again, the faster moving stream is in the

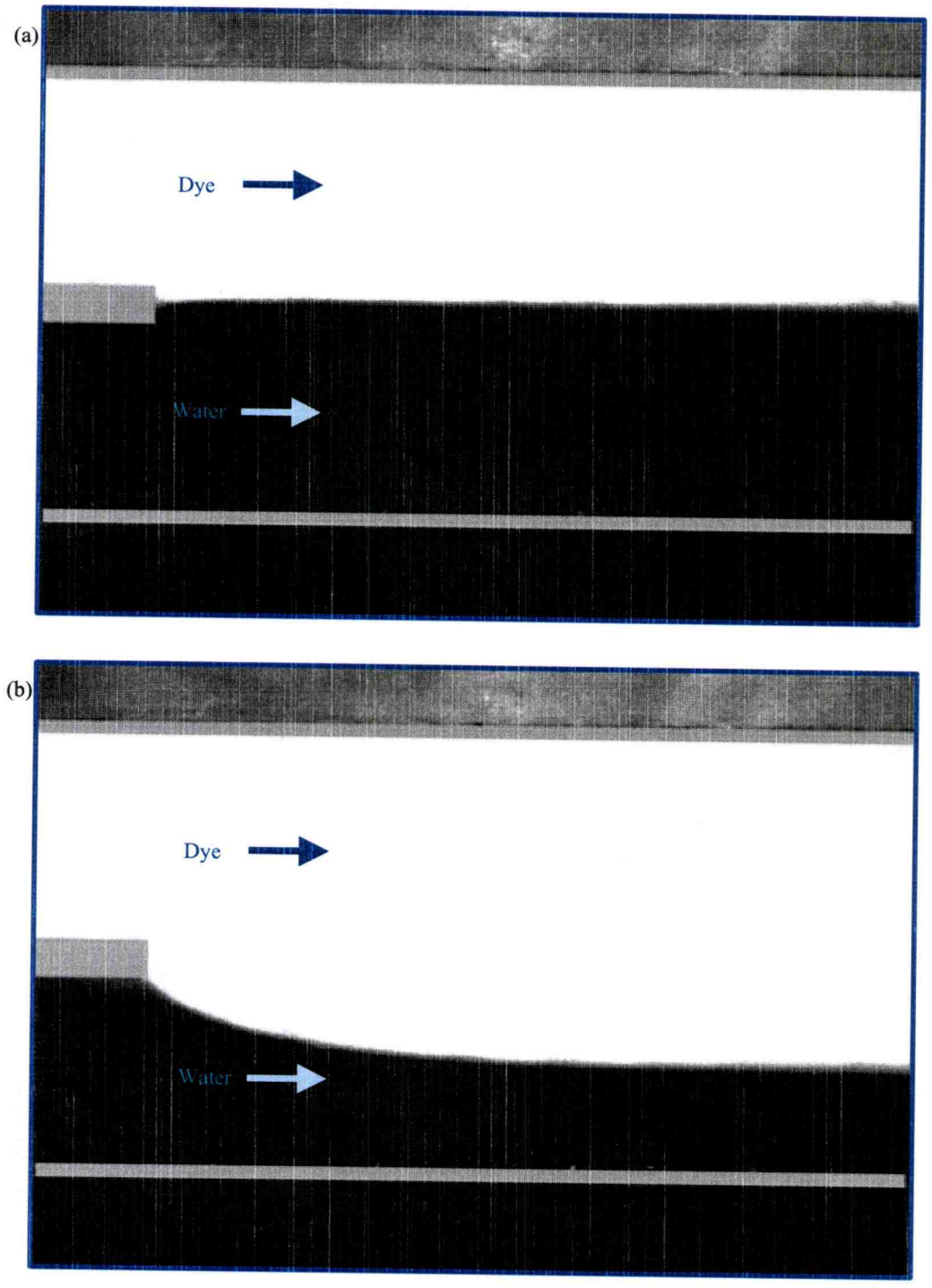

Figure 5.2
Close-up images of splitter plate region, Reynolds=1, Flow ratio one-to-one and one-to-three. The faster stream is located on top. The walls of the channel and the splitter plate are shaded out in gray. (a) one-to-one flow ratio, (b) one-to-three flow ratio.

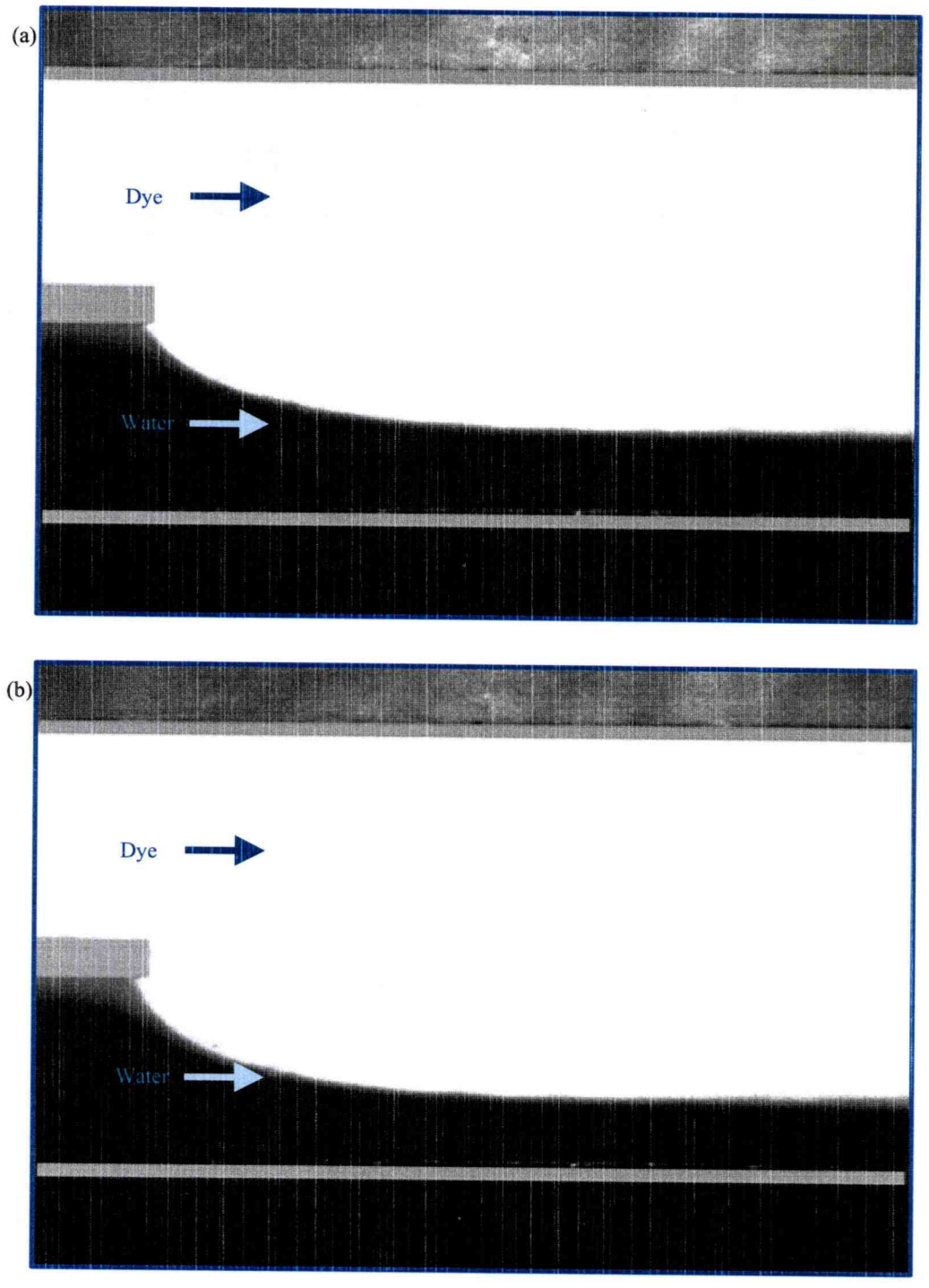

Figure 5.3
Close-up images of splitter plate region, Reynolds=1, Flow ratio one-to-five and one-to-seven. The faster stream is located on top. The walls of the channel and the splitter plate are shaded out in gray. (a) one-to-five flow ratio, (b) one-to-seven flow ratio.

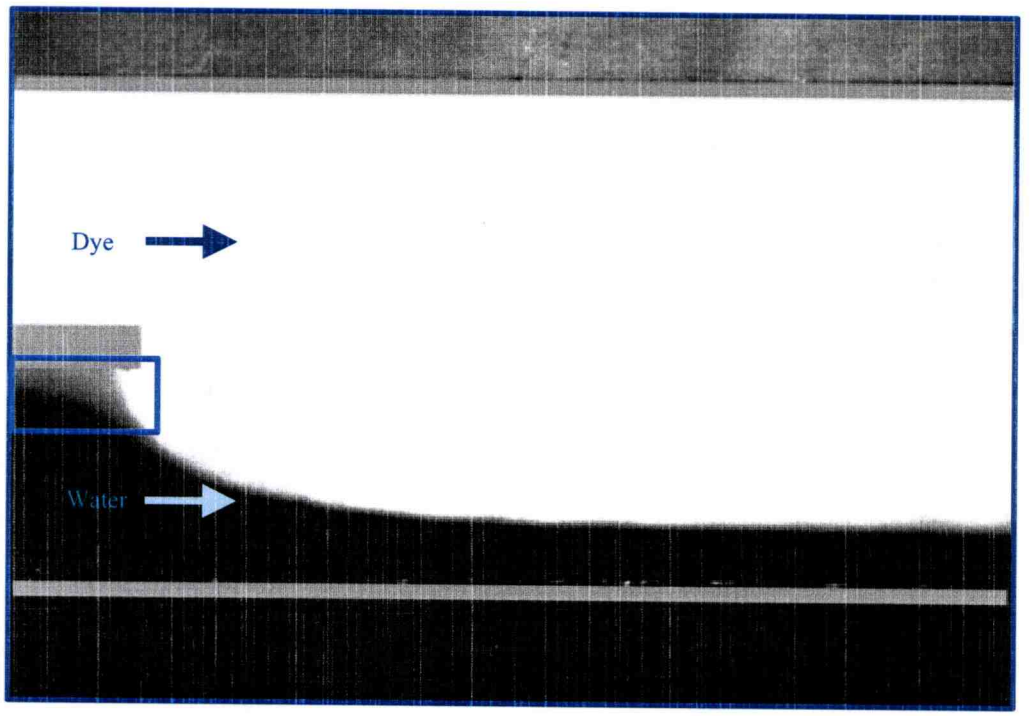

Figure 5.4
Close-up image of splitter plate region, Reynolds=1, Flow ratio one-to-nine. The faster stream is located on top. Note the presence of the gray area (blue box) indicating the presence of Rhodamine 6G Chloride.

top part of these figures, shown in white. As mentioned earlier, for flow ratios greater than unity, there is a large increase in lateral momentum which causes the faster moving velocity stream to expand just after the splitter plate. Consequently, the slower stream contracts. As the velocity ratios increase from one-to-three to one-to-nine, the momentum difference between the two streams increases, requiring a greater readjustment. Thus, the expansion of the faster moving dye stream occupies a greater portion of the channel. In order to quantify the amount of the expansion, the area ratios taken up by the respective streams were measured. For each flow condition, the area was estimated by measuring the width of the streams in the images and then multiplying it by the depth of the channel. These results are plotted on Figure 5.6 and identified as the measured results.

As a comparison, the area ratios were calculated for each flow ratio assuming inviscid, plug flow (Figure 5.5). This was done using a mass continuity analysis of the fast stream "streamtube" where the subscript "1" represents the inlet plane and "2" represents the outlet plane:

$$\rho_{1,f} v_{1,f} A_{1,f} = \rho_{2,f} v_{2,f} A_{2,f} . \tag{5.1}$$

Assuming constant density, the expression for the area taken up by the fast stream at the exit becomes:

$$A_{2,f} = \frac{v_{1,f} A_{1,f}}{v_{2,f}} . \tag{5.2}$$

Since the flow at the outlet plane ("2") for the inviscid case is considered to have a uniform velocity profile across the channel,

$$v_{2,f} = v_{2,f} = v_{2,total} . \tag{5.3}$$

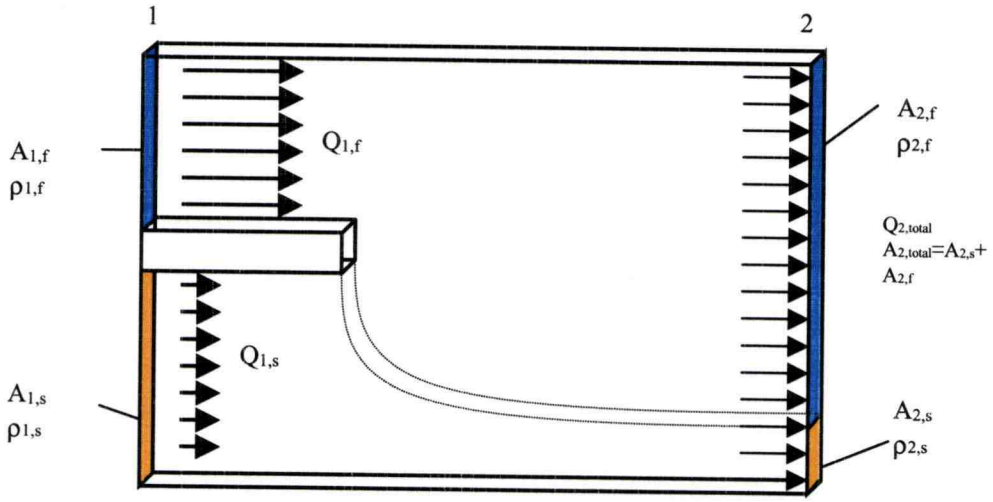

Figure 5.5
Diagram of inviscid flow analogy. The blue area represents the area that the faster moving stream would occupy given no shear, uniform flow across the channel.

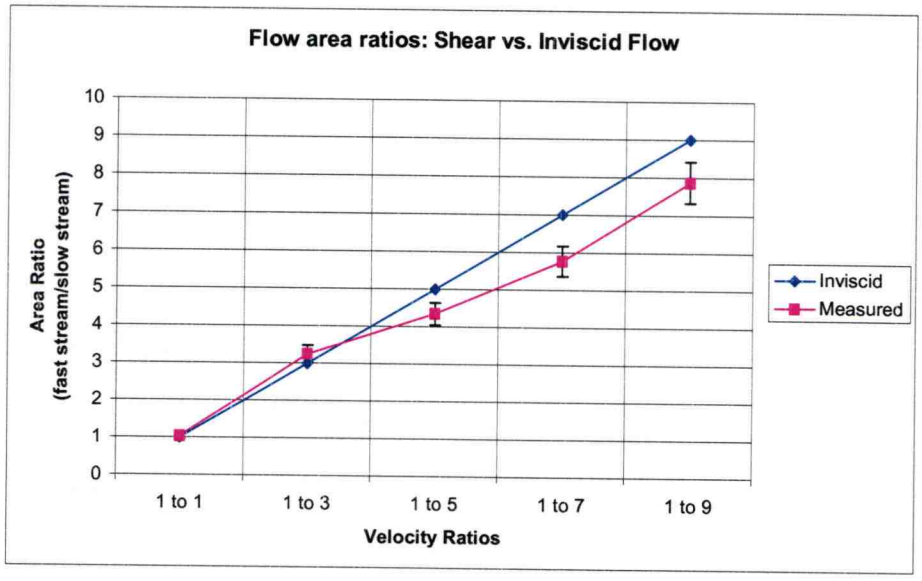

Figure 5.6
Area ratio vs. velocity ratio at downstream position for ideal (non-viscous) and measured (viscous) flow. The relative error is approximately 7%.

To find $v_{2,total}$, mass continuity is examined for the entire flow (constant density):

$$v_{1,f}A_{1,f} + v_{1,s}A_{1,s} = v_{2,total}A_{2,total}. \tag{5.4}$$

Therefore, an expression for the average velocity at the exit becomes,

$$v_{2,total} = \frac{Q_{1,f} + Q_{1,s}}{A_{2,total}}. \tag{5.5}$$

Substituting and rearranging, the expression for the area of the fast stream becomes:

$$A_{2,fast} = \frac{Q_{1,f}A_{2,total}}{Q_{1,f} + Q_{1,s}} = Q_{1,f}\left(\frac{A_{2,total}}{Q_{1,total}}\right) = \frac{Q_{1,f}}{v_{2,total}}, \tag{5.6}$$

which is simply a fraction based on the ratio of the flow rates. It can be seen from Figure 5.6, that at low flow ratios, the ideal and real flows behave similarly with respect to the amount of volume expansion occurring. However, as the flow ratios increase, the faster stream in the viscous case expands less than the ideal case. For example, for the one-to-seven flow condition, the faster stream in the real flow occupies 17% less of the channel than in the real case. This is taken to be an effect of the shearing forces on the faster moving fluid caused by both the walls of the channel and the slower stream.

The other noticeable aspect of these images in Figures 5.2 through 5.4 is that at flow ratios above one-to-three, a gray region is present next to the splitter plate in the slower stream. Initially, this was thought to be a consequence of either an advective backflow or simple diffusion from the faster stream. This will be discussed in the next section.

Particle Image Velocimetry results

This section presents the results obtained during the PIV portion of the study. Images were taken for flow ratios of one, three, five, seven, and nine. In each case, the flow rates were adjusted such that the Reynolds number in the chamber was maintained at either one or ten. Each of the velocity fields presented is an average of 5-10 individual velocity fields. The results are organized into four parts. In the first part, the fully developed velocity profile is examined. The second part discusses the interaction of the flow at the end of the splitter plate based on Reynolds number one. In the third section, the effect of varying Reynolds number is examined. The final part considers the length for flow development.

Velocity profile in rectangular microchannel

In order to examine the preface that the two fluid streams approach the splitter plate end as fully developed streams, the measured velocity profiles upstream of the splitter plate were plotted. The coordinates utilized in this study are shown in Figure 5.7. Since the two dimensional velocity profile for a rectangular channel is computationally complex, a simplified approximation of the profile for fully developed flow with no-slip boundary conditions is given in Shah and London (1978) as:

$$\frac{u}{u_{max}} = \left[1-\left(\frac{y}{b}\right)^n\right]\left[1-\left(\frac{z}{a}\right)^m\right], \qquad (5.7)$$

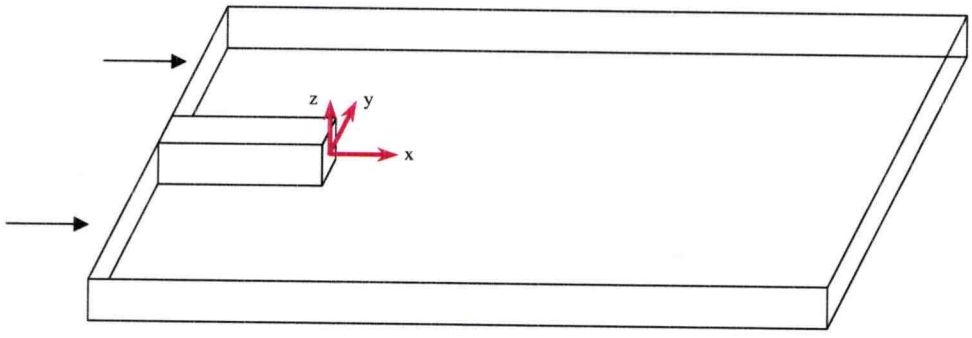

Figure 5.7
Coordinate system employed in this study. The origin is located at the center of the tip of the splitter plate.

where u is the downstream velocity component, a and b are half the width and depth of the channel, respectively, y is the coordinate in the depth-wise direction, and z is the coordinate in the width-wise direction, with the origin at the center of the channel. The constants, m and n are given as:

$$\begin{aligned} m &= 1.7 + 0.5\left(\frac{b}{a}\right)^{-1.4} \\ n &= 2 \qquad\qquad \text{for} \left(\frac{b}{a}\right) \leq 1/3 \end{aligned} \quad . \tag{5.8}$$

Therefore, for the microchannel under investigation, m=10.12 for the faster channel and m=9.39 for the slower channel (due to the small difference in cross-sectional area). For each stream (faster and slower), the stream-wise velocity profiles between x = -324 μm and –253 μm were non-dimensionalized and then averaged for each channel using the data from each flow ratio for Reynolds number one. The result is shown in Figure 5.8, along with the analytical profiles from above with z = 0 (channel centerline). The analytical solutions for the two channels are very similar to each other. As can be seen, the experimentally obtained velocity profile tends to show a smaller velocity gradient near the walls relative to the analytical solution. Also, the viscous effects appear to propagate further into the center of the channel. One partial explanation for this discrepancy could be due to the inherent problems associated with the introduction of flow tracer particles and their interaction with the wall effects (Meinhard *et al.*, 1999). Another reason could stem from the effective depth of field of the visualization system. Since the design of the microchannel device does not permit the use of a laser sheet, the depth-wise resolution is based on the focal depth of the optics system. Coupled with this is the premise that particles that are not in the focal plane will not give off enough

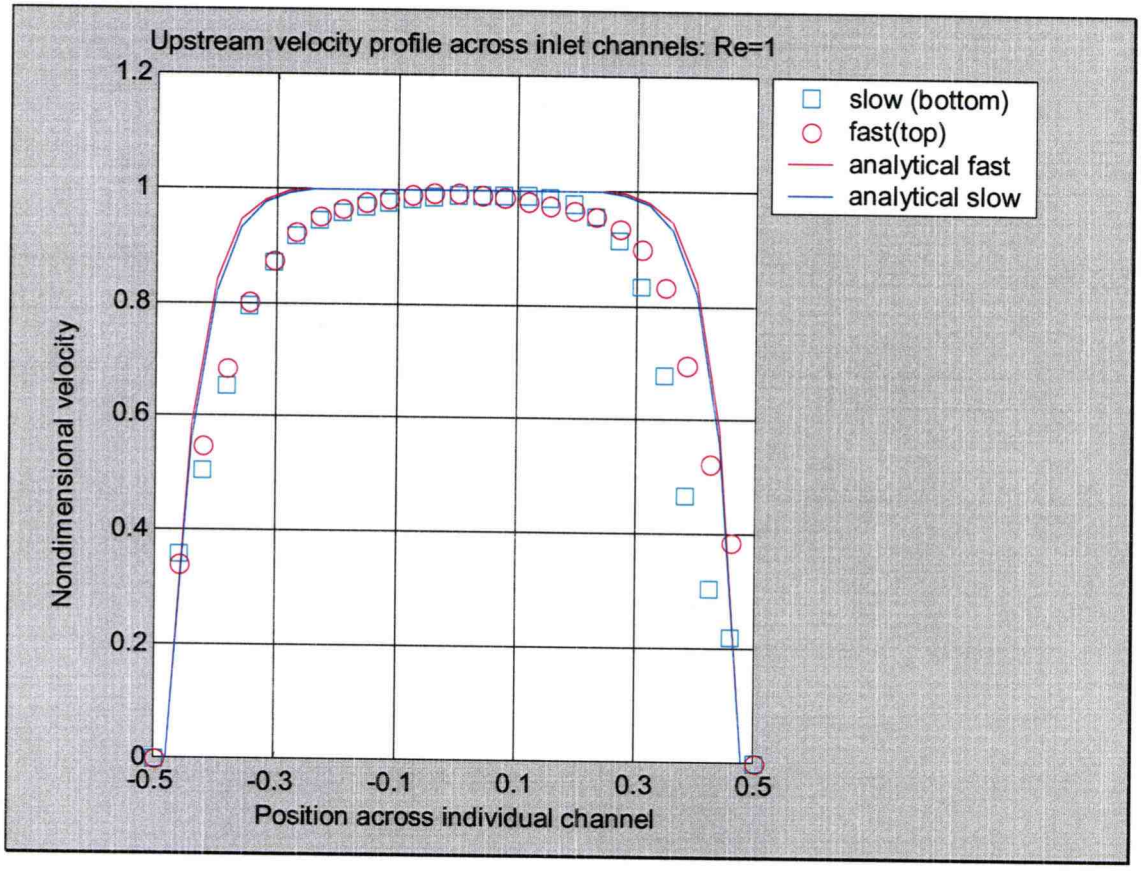

Figure 5.8
Averaged velocity profile far upstream of splitter plate end. Profiles are averaged between downstream positions, x=-324 and –253 um. "Slow" refers to the bottom inlet channel and "Fast" refers to the top channel. The analytical profiles are also included from Shah and London (1978) given their respective channel width and depths. The uncertainty for the slow and fast streams are estimated to be approximately 0.18 and 0.063, respectively, based on the calculated uncertainties in the velocities (See Appendix).

fluorescence for the cross-correlation to place much weight on their influence on the resulting velocity vector. However, this is not always the case, which would increase the actual depth of field. The depth of field for the system was found to be approximately 11 μm, which would encompass almost 20% of the channel depth. Therefore, it is possible that "centerline" profiles that were obtained may be contaminated by the presumably slower flow that is near the top and bottom of the channels.

Flow interaction at end of splitter plate

Figure 5.9 and Figure 5.10 show the velocity vector field plots of the region surrounding the splitter plate for flow ratios of one-to-one and one-to-nine, respectively, at a main channel Reynolds number of one. For clarity, the individual vectors are all scaled automatically by Matlab in order to minimize overlapping vectors. As would be expected, the flow field in the one-to-one flow condition is relatively symmetric along the centerline of the channel. The flows from the individual channels both expand slightly toward the centerline and the flow "bends" around the corner of the splitter plate. Then the flow continues to travel parallel toward the exit. This behavior is similar to what was found in the fluorescent dye study. The two streamlines plotted in the figure also emphasize the behavior with each line veering toward the center of the channel after the end of the splitter plate. In contrast, the flow for the one-to-nine flow condition is asymmetric with respect to the centerline. The flow region near the splitter plate in the faster stream tends to flow laterally into the slower moving stream, eventually being redirected back parallel to the channel by the momentum of the slower moving stream.

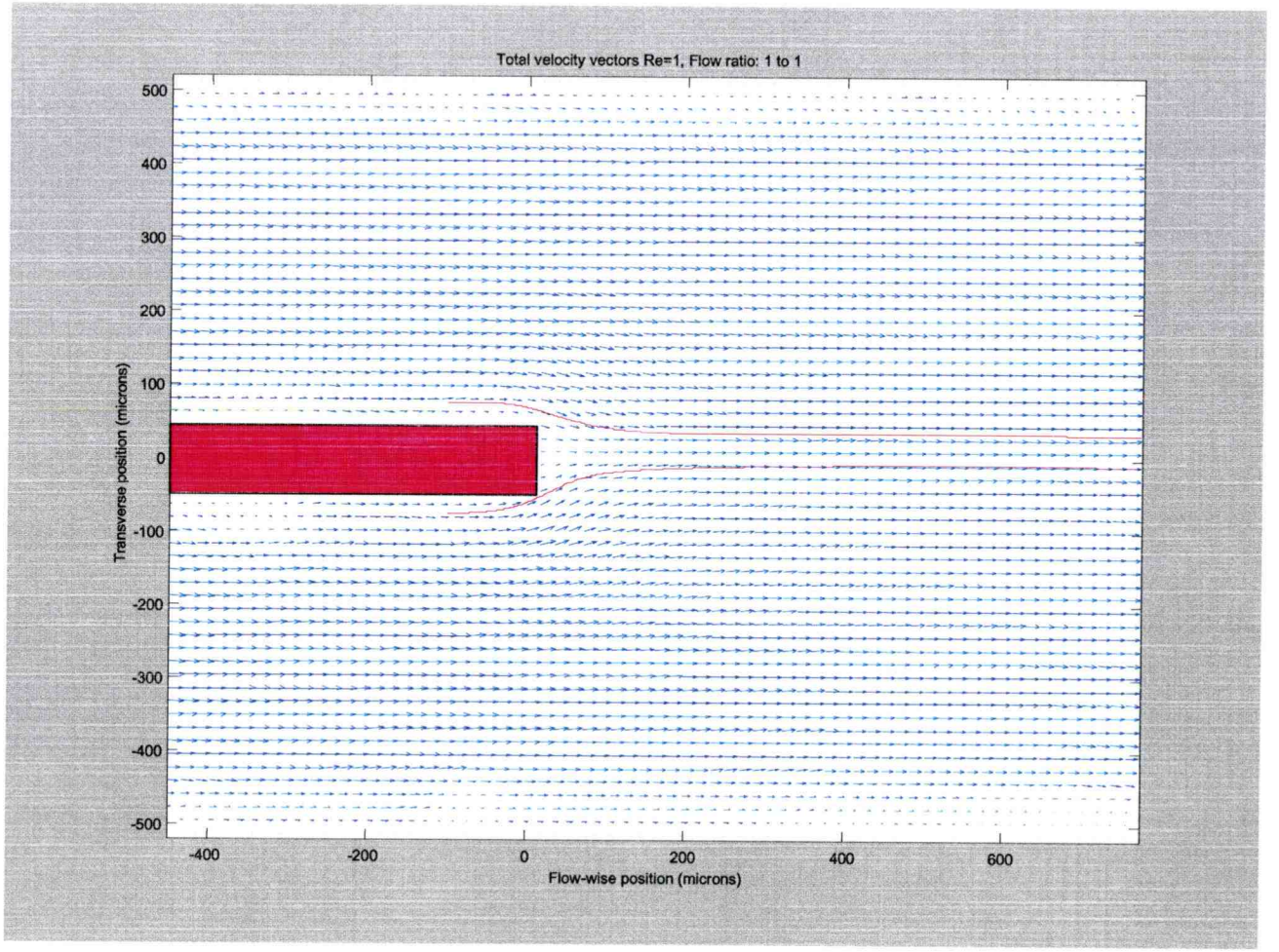

Figure 5.9
Velocity vector plot for Reynolds = 1, Flow ratio of one-to-one. The faster stream is above the splitter plate (red). Two streamlines are shown orginating at (-100,75) μm and (-100,-75) μm.

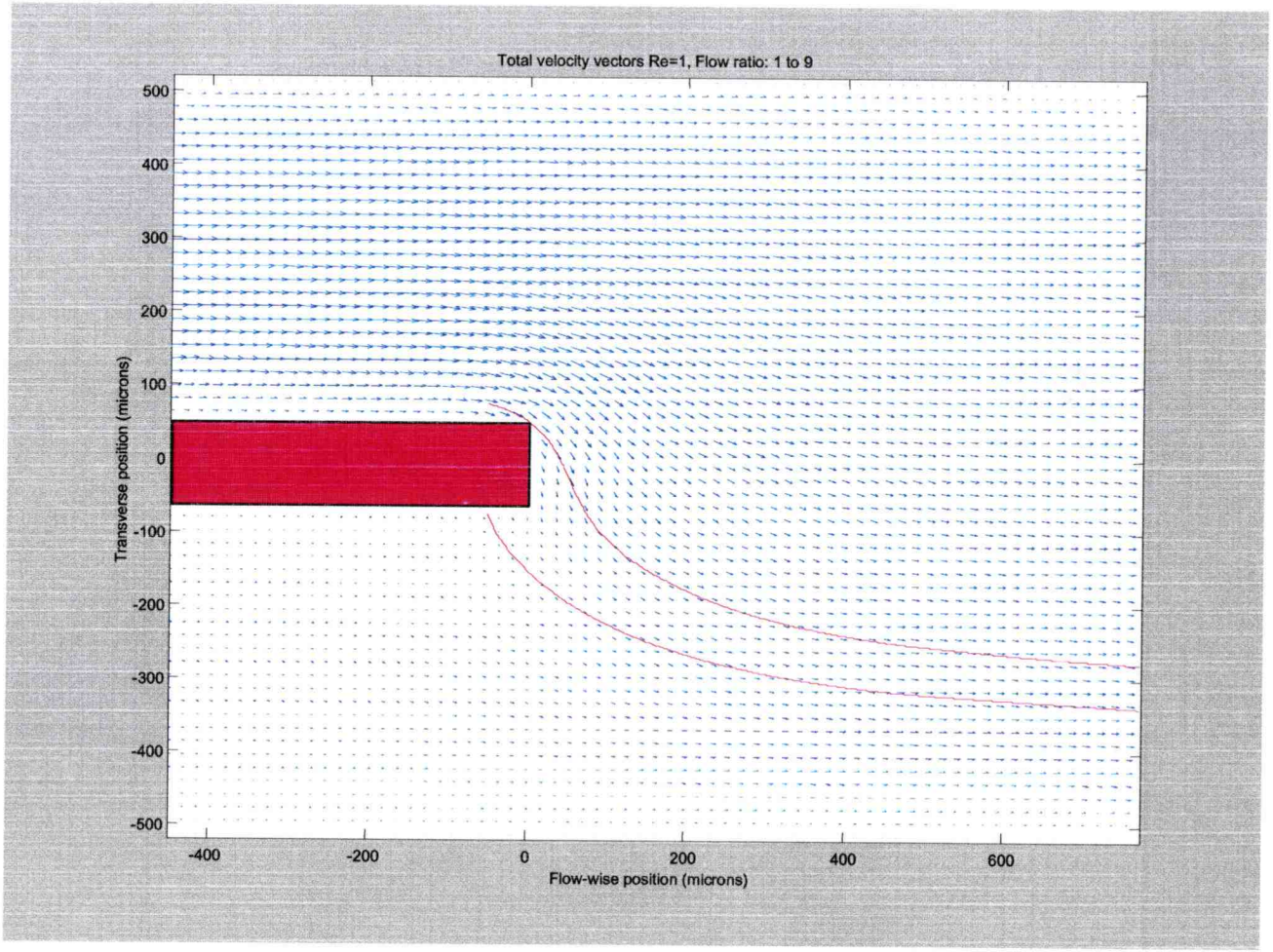

Figure 5.10
Velocity vector plot for Reynolds = 1, Flow ratio of one-to-nine. The faster stream is above the splitter plate (red). Two streamlines are shown at (-50,75) μm and (-50, -75) μm.

Again, the streamlines demonstrate this asymmetry. The streamlines originate at the same distance from the splitter plate as those in Figure 5.9, but have very different behaviors immediately after the end of the splitter plate. This general pattern also holds true for the one-to-three, one-to-five, and one-to-seven flow ratio conditions, with the lower ratios demonstrating less of a lateral shift.

Another representation of the full field velocity data is given in Figure 5.11. In these images faster flowing fluid is indicated in red, and slower moving fluid is in blue. Each image is scaled identically. For flow ratios greater than unity, most of the top channel is occupied by faster moving fluid upstream of the splitter plate end. However, as the two streams merge, the viscous interaction between the faster and slower moving fluids acts to accelerate the slower moving fluid and decelerate the faster one. Thus, in the top half of the channel, the fluid closer to the channel wall maintains its higher velocity further downstream than the fluid near the centerline. This is illustrated by the observation that the yellow section extends further downstream in the region closer to the top wall relative to the center. Further downstream, the two streams approach a common velocity. The acceleration of the faster moving fluid and the corresponding deceleration of the slower moving fluid as the flow progresses downstream can be seen in the stream-wise velocity profiles in Figure 5.12b. The velocity profiles in Figure 5.12 are normalized to the maximum velocity at each cross-section in order to provide an uncluttered fit. Looking at the flow ratio of one-to-one (Figure 5.12a), once the flow is past the splitter plate, there is no longer a "momentum sink" in the form of a solid wall. Thus, the momentum of the bulk flow of the individual streams propagates toward the centerline of the channel, accelerating the centerline flow. Similarly, for the one-to-nine

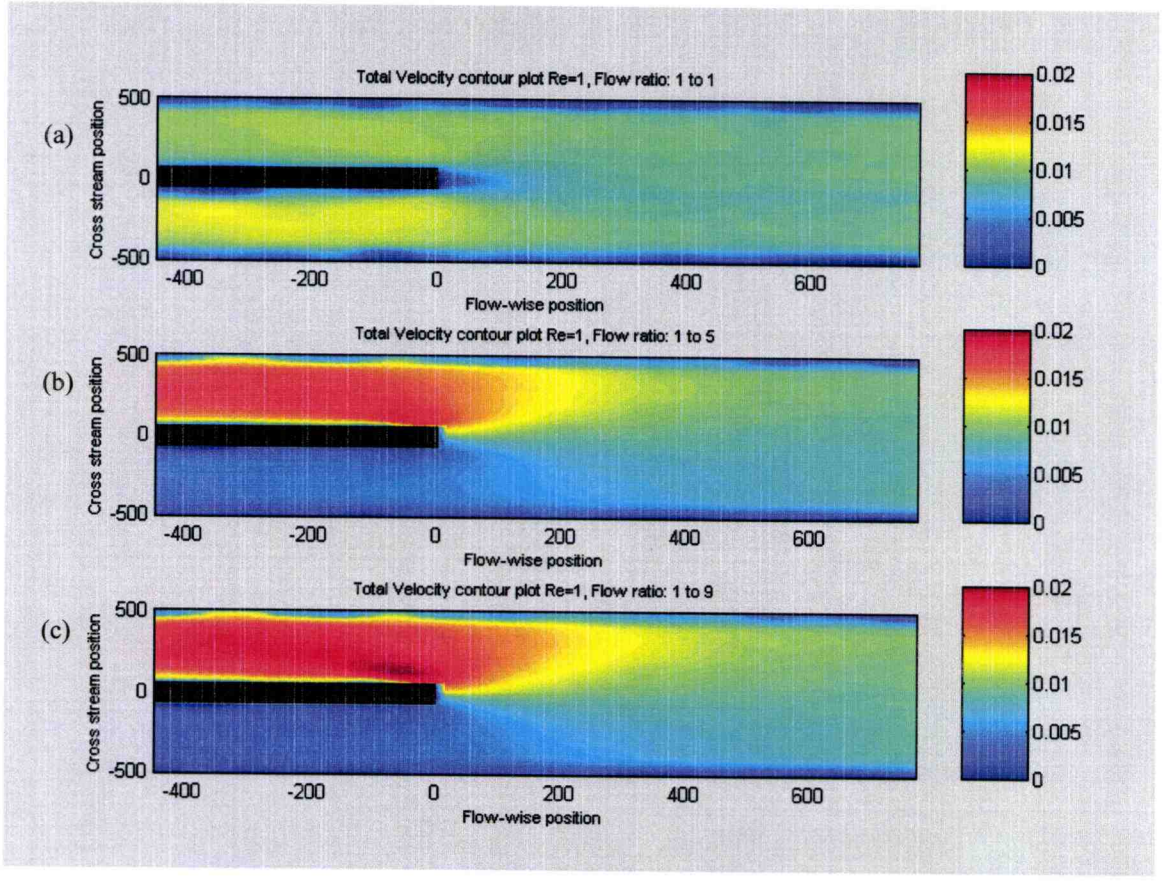

Figure 5.11
Velocity contour plots for Reynolds number = 1 flow condition. Flow ratios: (a) one-to-one, (b) one-to-five, (c) one-to-nine. The units of velocity are m/s.

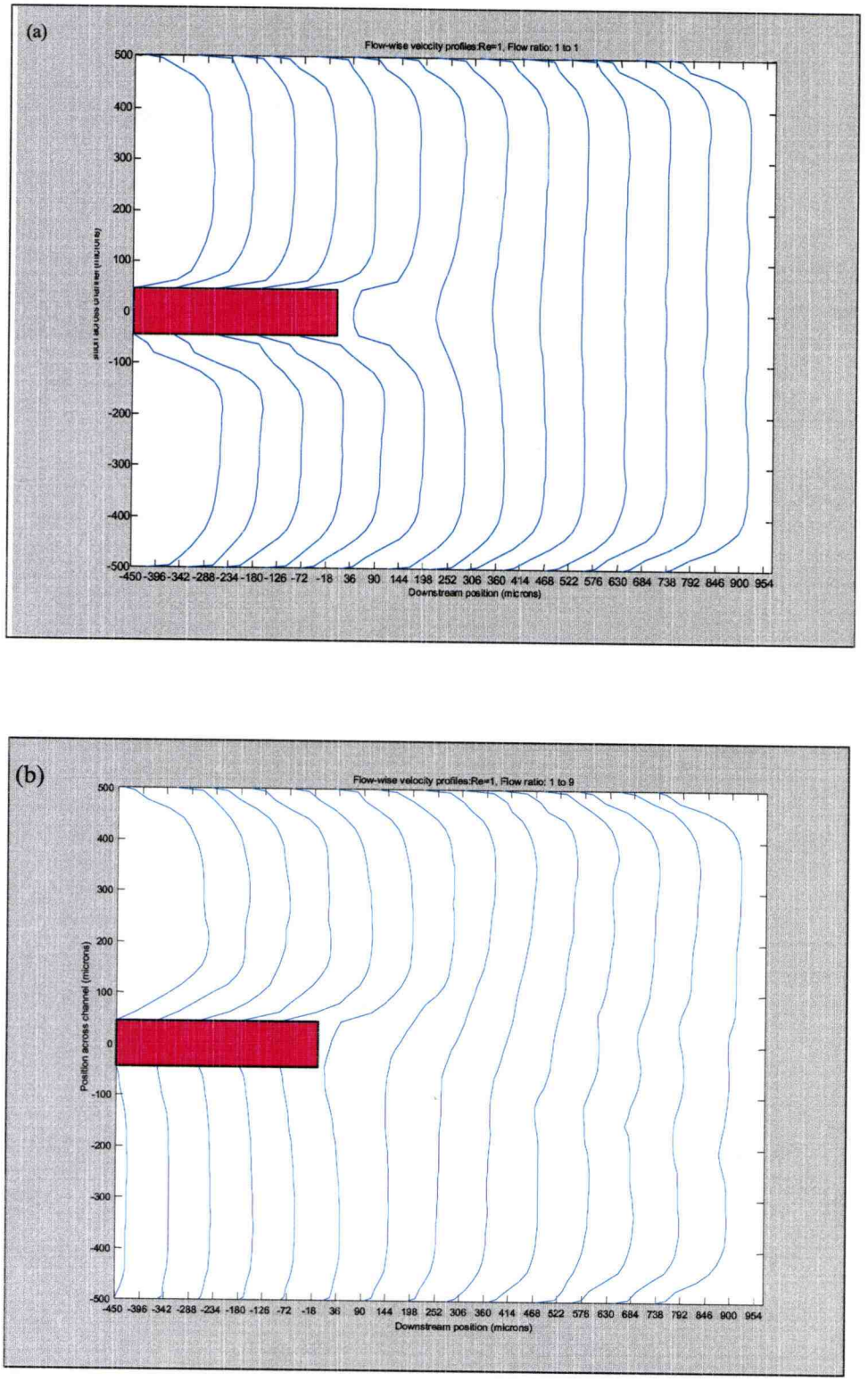

Figure 5.12
Non-dimensionalized (u/u_{max}) velocity profiles across the channel, Reynolds = 1. (a) one-to-one flow ratio, (b) one-to-nine flow ratio. The red region represents the splitter plate.

flow ratio, the local velocity minimum between the two streams dissipates rather quickly, "pulling" the slow stream forward and the faster stream backward.

Figure 5.13 presents the stream-wise velocity profiles in a more detailed fashion at more positions down the length of the channel. For the one-to-one flow ratio case (Figure 5.13a), a slight asymmetry can be seen between the two channels. The bottom channel (the "slower" one in the other ratios) has a slightly higher maximum velocity than the top one. Based on maximum velocity, the bottom channel is roughly 8% faster than the top channel. However, as will be seen later, they both have roughly the same average velocity. This bias is fairly consistent with the observation that the bottom channel is approximately 6% smaller in width than the top one. This inconsistency is most likely a result of imperfections in the channel (i.e. introduction of grease and misalignment of the splitter plate). The other feature to note from Figure 5.13a is the fact that, as the flow passes the tip of the splitter plate (at x=0 μm), the position of the local velocity minimum between the two streams remains along the centerline of the channel. For the velocity profiles at x=18, 54, 90, 126, and 162 μm, the minimum remains at the y=0 μm centerline position until it disappears into the fully developed profile. In Figure 5.13b and c, however, these same local minimums shift slightly away from the centerline towards the slower moving stream as the flow progresses downstream. For the one-to-five ratio, (Figure 5.13b), the local minimum moves from approximately half the width of the splitter plate (approximately 45 μm) at x=18 μm to approximately -125μm from the centerline at x=162 μm downstream. Similarly, for the one-to-nine flow ratio (Figure 5.13c), the local minimum moves from roughly the same transverse position at x=18 μm to approximately 175 μm away from the centerline at x=162 μm. This is similar

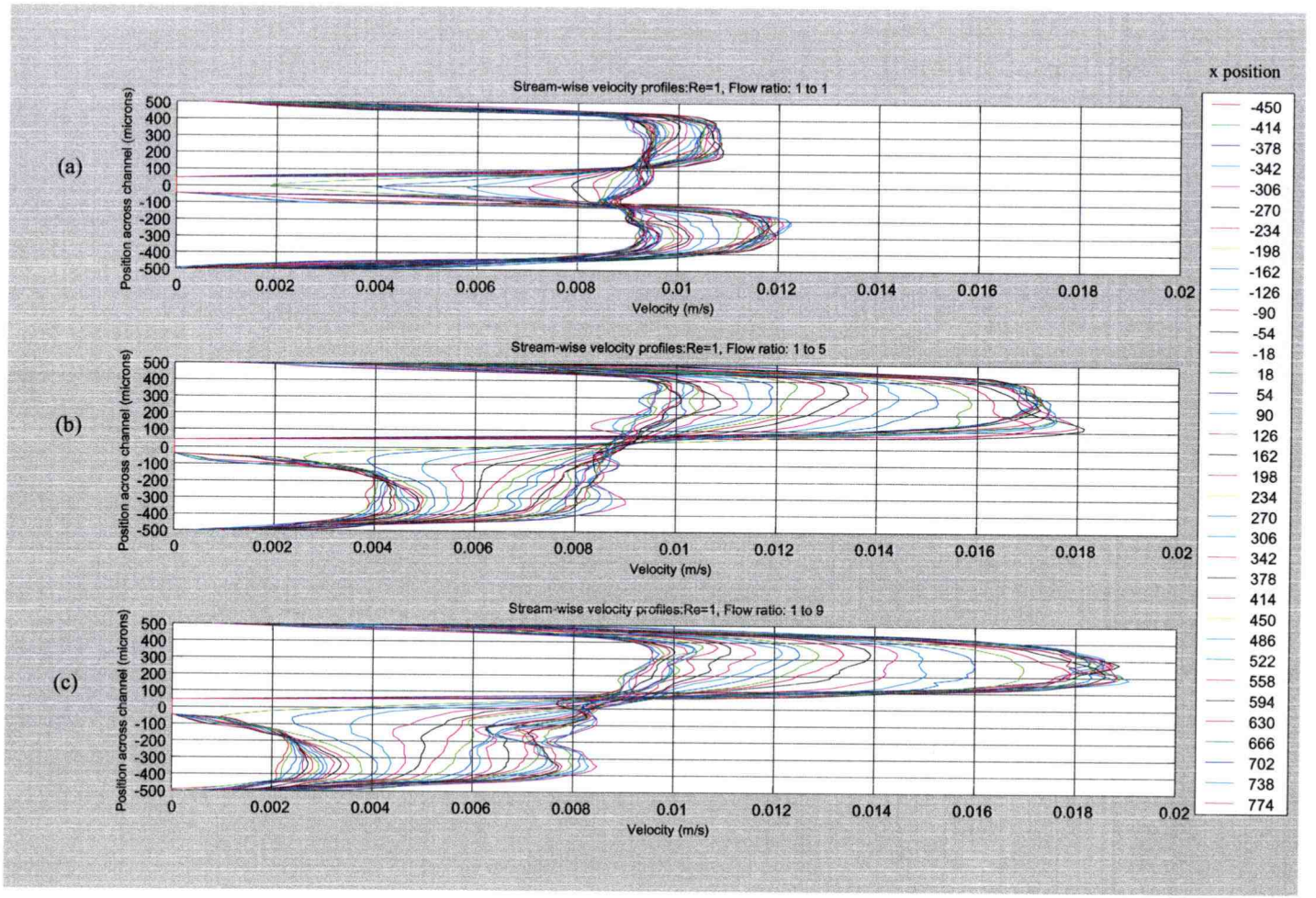

Figure 5.13
Stream-wise velocity profiles- various flow ratios, Reynolds = 1. Each line represents the velocity profile at a particular x location. (a) Ratio one-to-one, (b) Ratio one-to-five, (c) Ratio one-to-nine.

to the propagation of a wave, since the shear forces decelerate the faster moving fluid while simultaneously accelerating the neighboring slower fluid.

As noted in the previous figures, a local minimum occurs in the stream-wise component of velocity just following the end of the splitter plate. However, as can be seen in Figure 5.14, the cross-stream component of velocity actually has its maximum magnitude in the region just after the splitter plate. In this figure, the cross-stream velocity components are plotted across the channel for different downstream (x) positions. For the one-to-one flow ratio (Figure 5.14a), the flow upstream of the splitter plate has very little cross-stream component (there is some, but this is most likely due to irregularities in the splitter plate), but once the flow passes the end of the splitter plate, the magnitude of the velocities increase and then fade away. The opposing signs of the cross-stream velocities indicate that the streams from the two inlet channels actually flow towards each other and then the cross-stream component fades away. In Figure 5.14b and Figure 5.14c, a similar phenomenon occurs except that all of the flow is only in one direction. As can be seen in the figure, the one-to-five ratio condition has a higher maximum cross-stream velocity component than the one-to-nine condition. However, as will be discussed in the next section, this behavior is not consistent at higher Reynolds numbers. This suggests that, at low Reynolds numbers, there may be an optimum velocity ratio for maximizing the cross-stream velocity magnitude.

Another trend is the shifting of the downstream position of the maximum cross-stream velocity. This can be seen in Figure 5.15 as well as in Figure 5.16, which zooms in on the region just beyond the end of the splitter plate. Figure 5.15a clearly illustrates the symmetry of the opposing cross-stream flows. In Figure 5.16b-e, an ellipse roughly

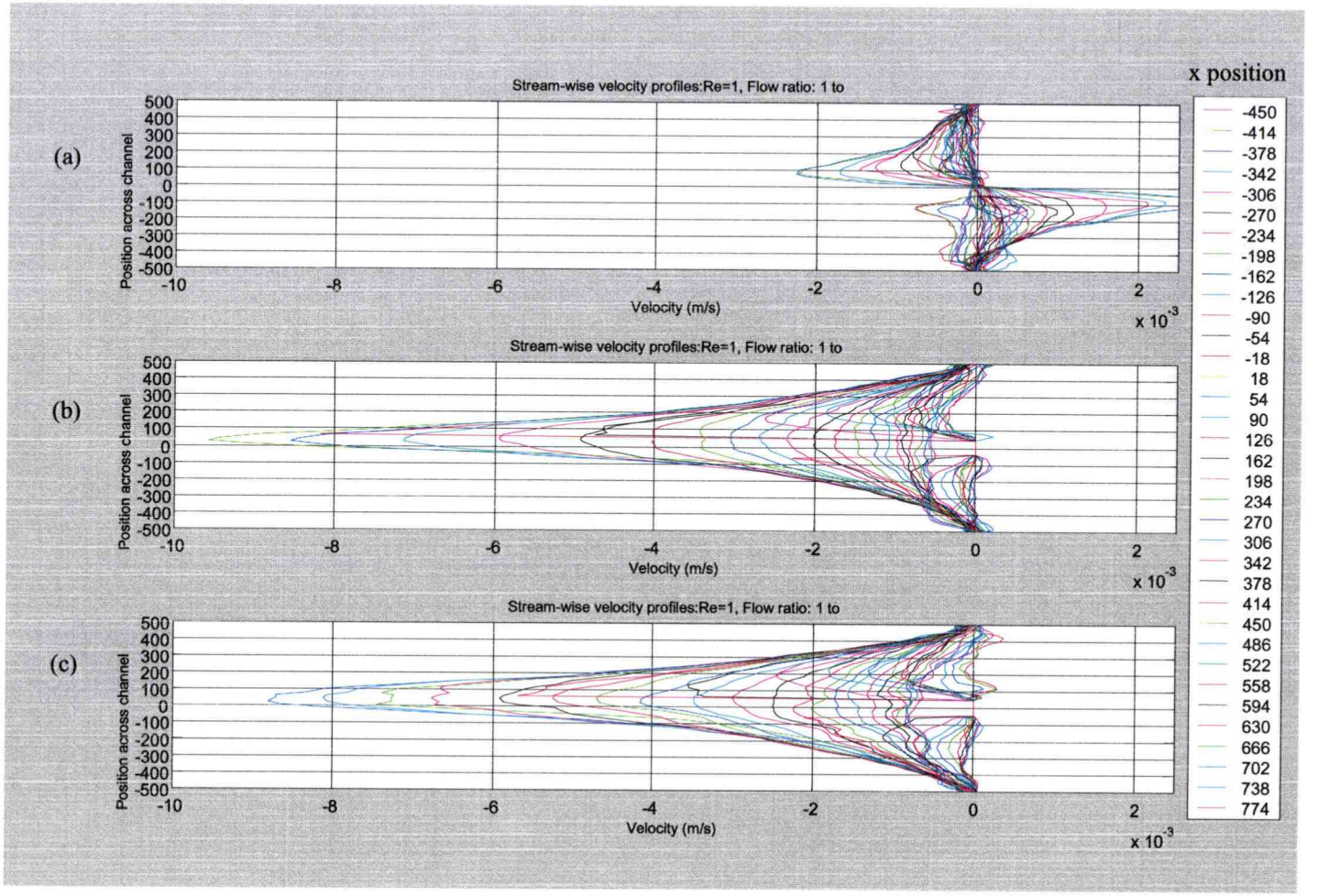

Figure 5.14
Cross-stream velocity profiles- various flow ratios, Reynolds = 1. Each line represents the velocity profile at a particular x location. (a) Ratio one-to-one, (b) Ratio one-to-five, (c) Ratio one-to-nine.

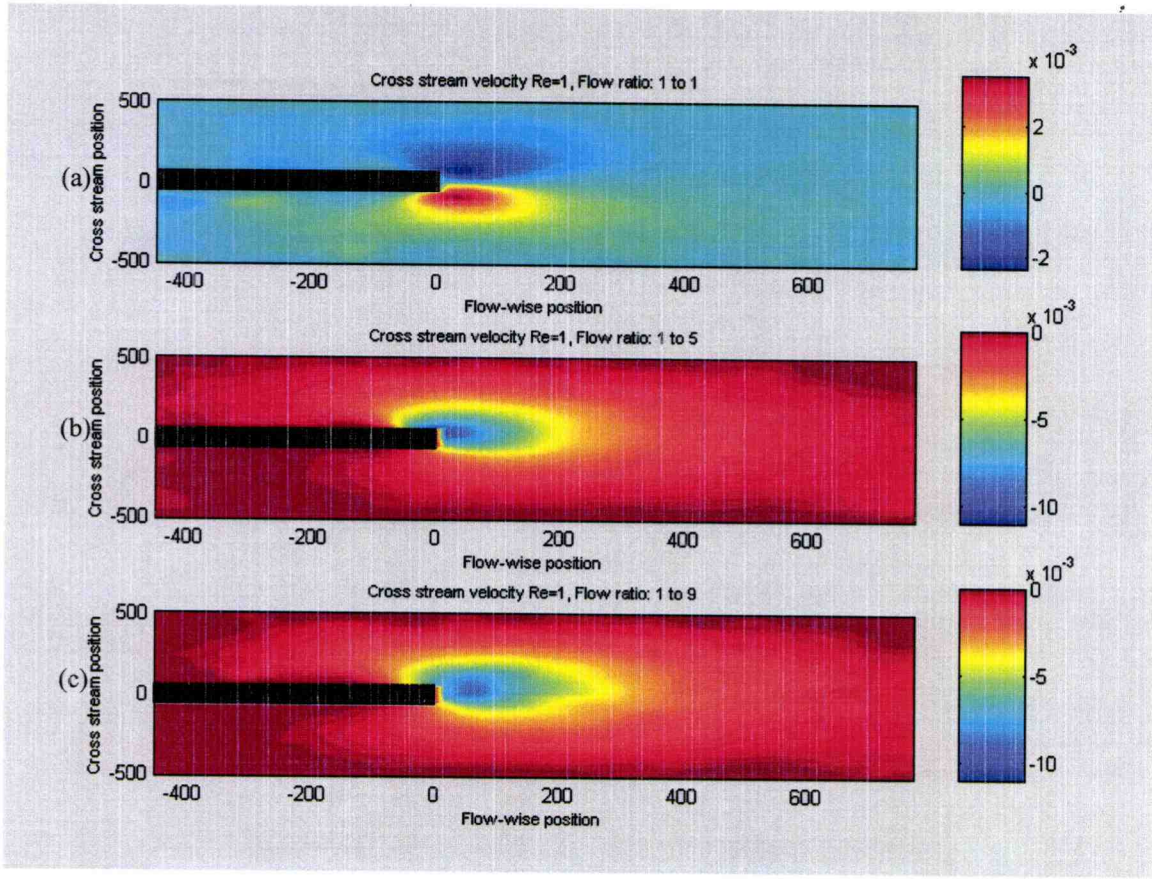

Figure 5.15
Cross-stream velocity contour plot, Reynolds = 1. The splitter plate is indicated in black (a) Flow ratio one-to-one, (b) Flow ratio one-to-five, (c) Flow ratio one-to-nine

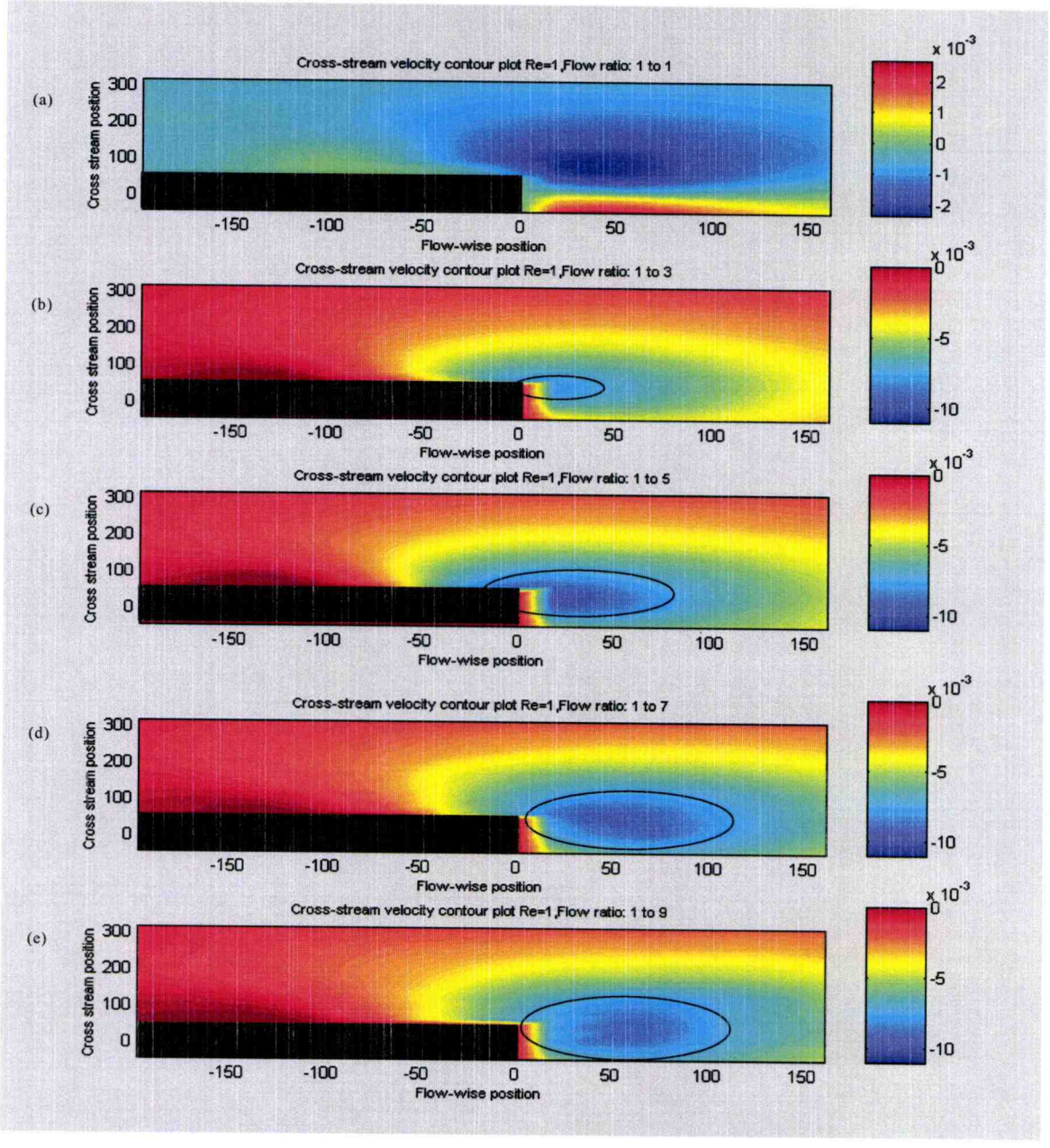

Figure 5.16
Cross-stream velocity contour plot, Reynolds = 1 (zoomed in). (a) Flow ratio one-to-one, (b) one-to-three, (c) one-to-five, (d) one-to-seven, (e) one-to-nine. The splitter plate is in black. Note the movement of the maximum velocity region downstream as velocity ratio increases.

defines the region of fluid with the greatest cross-stream velocity. By taking the geometric center of these ellipses, it can be seen that the center shifts downstream from approximately x=20 μm at a flow ratio of one-to-three to approximately 60 μm at a flow ratio of one-to-nine. A possible explanation for this behavior could be that as the flow ratios increase, the increased convective motion of the fluid results in a spatially delayed lateral momentum exchange.

Figure 5.17 shows the region below the splitter plate in the slow stream at a higher resolution scale. The reason for examining this region stems from the presence of the gray region in Figure 5.4 indicating the presence of Rhodamine 6G Chloride from the faster stream in the slower stream. Initially, based on preliminary numerical data (Oak *et al.,* 2001) this was thought to be the result of an advective backflow around the splitter plate from the higher pressure in the dye stream to the lower pressure in the water stream. However, the PIV data does not explicitly show this recirculation. Figure 5.17 does, however, show a region of very slow velocity on the underside of the splitter plate at higher flow ratios. The size and shape of this depressed flow area roughly corresponds to the shape and location of the gray region. Therefore, the possibility of the "diffusion velocity" of the Rhodamine 6G Chloride being high enough to overcome the advective velocity of the fluid was considered.

In order to identify a "diffusion velocity," an analogue of the temperature solution for a transient, one-dimensional, semi-infinite solid was employed (Incropera and Dewitt, 1996). The solution has the following form:

$$\left(\frac{C(\phi,t)-C_{\phi}}{C_i-C_s}\right)=\mathrm{erf}\left(\frac{\phi}{2\sqrt{Dt}}\right), \tag{5.9}$$

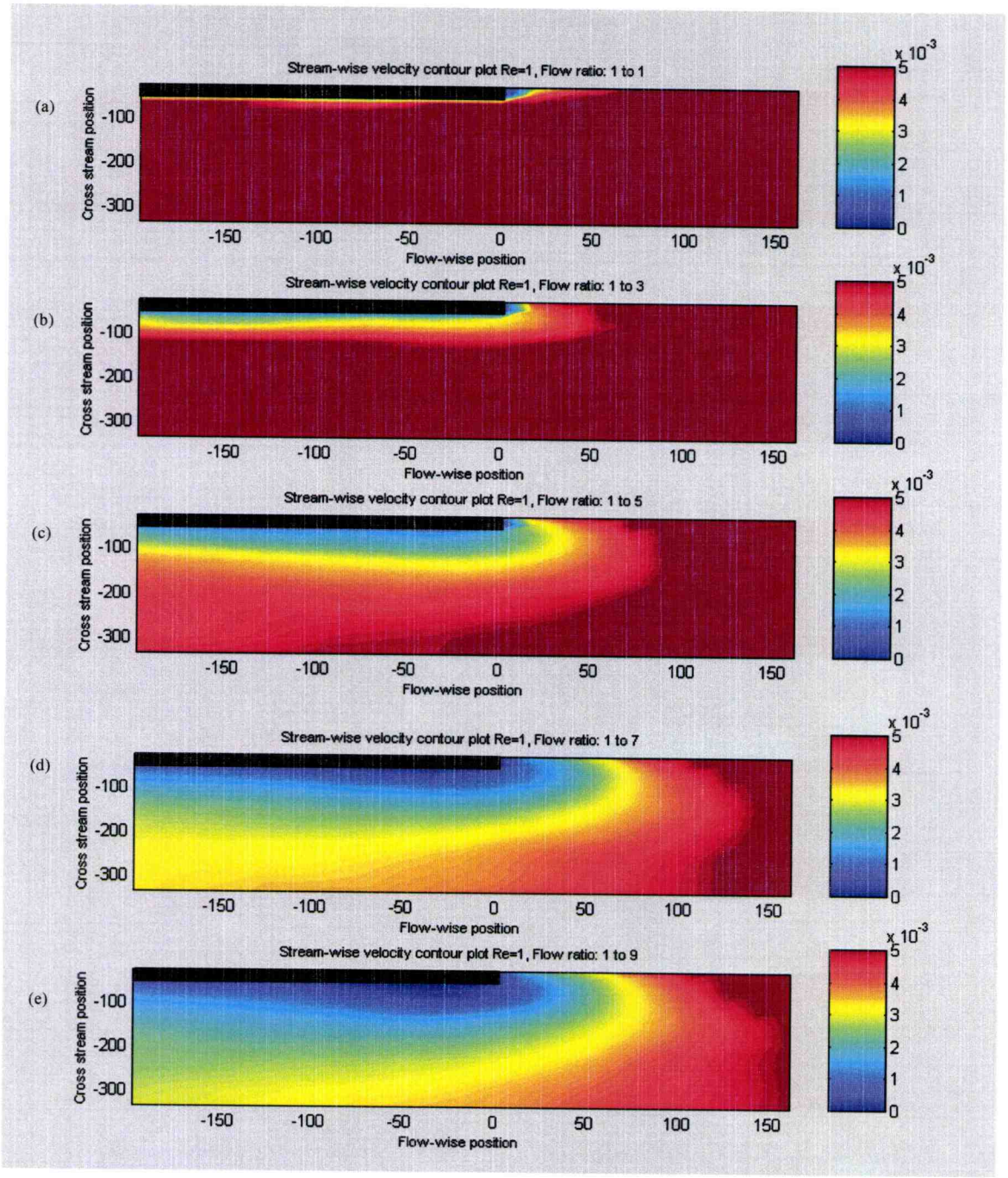

Figure 5.17
Stream-wise velocity contour plot, Reynolds = 1 (zoomed in). The splitter plate is indicated in black. (a) Flow ratio one-to-one, (b) one-to-three, (c) one-to-five, (d) one-to-seven, (e) one-to-nine.

where ϕ is the position coordinate, C is the concentration, and the subscripts "s" and "i" refer to the "surface" and the initial concentrations, respectively. To do an order of magnitude analysis, the relative concentration at approximately 200 μm upstream from the interface between the dye and water was estimated from Figure 5.4 to be approximately one-half the concentration of the dye stream (C_s). Therefore, assuming $C(\phi=200\mu m)$ to be 0.5 and $C_s = 1$, and $C_i = 0$, the time solution was found to be approximately 144 seconds. Dividing the expected diffusion distance, 200 μm, by the time, 144 seconds, the "diffusion velocity" was then estimated to be only on the order of 10^{-6} m/s. Unfortunately, from the PIV data, the velocities in the dark blue region are on the order of 10^{-4} m/s, two orders of magnitude greater than the diffusion velocity. Therefore, this would suggest that the downstream advection would dominate over the upstream diffusion and there would be no mechanism for the Rhodamine 6G Chloride to access the region. However, from an uncertainty analysis it was found that the PIV data is not very reliable at such small velocities, with the uncertainty in velocities in that region being on the same order of magnitude as the velocity values themselves. Given an image-to-image time separation of 400 μs, an individual seed particle would only travel about 0.04 μm. This distance is much smaller than the predicted resolution of the optical setup and the PIV software algorithm. Therefore, the reliability of the data obtained from that region may be in question. Therefore, there still exists is a strong possibility that a re-circulation is actually occurring around the splitter plate. This speculation is further reinforced by the observation that the dye stream in Figure 5.4 actually begins to encroach upon the region upstream of the splitter plate in the slower moving stream.

Figure 5.18 shows the region above the splitter plate in more detail. It can be seen that there is a region of accelerated fluid near the splitter plate in this region at higher flow ratios. In this experimental setup, the syringe pumps supply the pressure required to obtain the desired flow rate. Given that the flow is fully developed in the region before the end of the splitter plate, the pressure drop must be higher for the faster moving stream than for the slower one. The presence of the splitter plate maintains this pressure imbalance between the two streams. However, once the streams flow past the splitter plate and merge, there is no longer a mechanism to maintain this pressure imbalance. Consequently, as the flows merge, the imbalance causes the fluid nearest the splitter plate in the faster moving stream to accelerate and expand into the slower moving stream. This expansion, however, also causes the bulk velocity of the faster moving stream to decrease (decelerate). In addition, as mentioned earlier, the region of fluid in the slower stream that is just upstream of the expansion decelerates as well. Therefore, as a result of the pressure driven acceleration and deceleration, the streams no longer have their fully developed velocity profiles when they enter the mixing region.

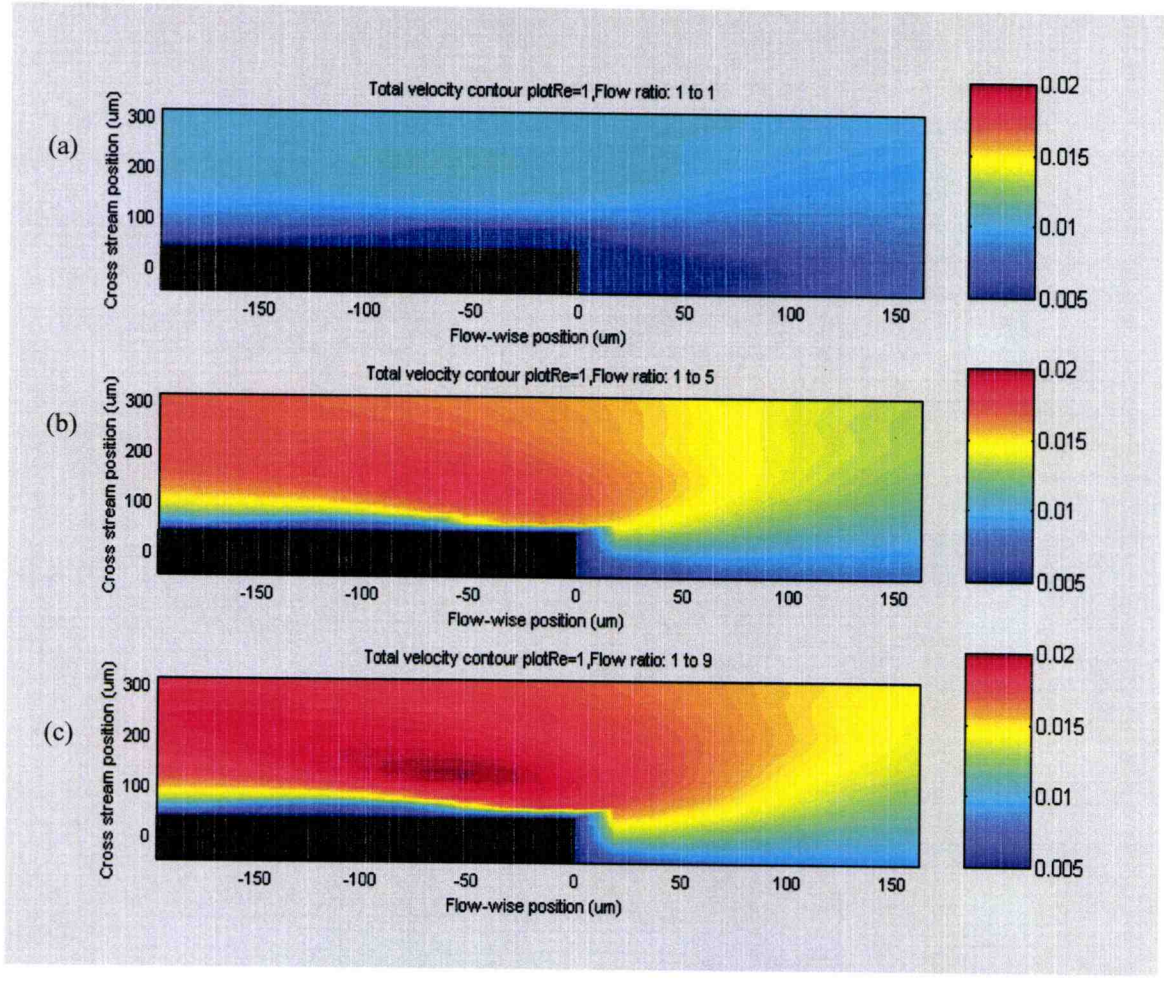

Figure 5.18
Total velocity contour plot, Reynolds = 1 (zoomed in). The splitter plate is indicated in black. (a) Flow ratio one-to-one, (b) one-to-five, (c) one-to-nine.

Effect of Reynolds number

PIV data were also obtained at a Reynolds number of ten for the same flow ratios as for the case of Reynolds number of one, using the same channel. In order to make a comparison between the data, streamlines were drawn at several points in the flow field and the images were overlaid on each other (Figure 5.19, Figure 5.20, and Figure 5.21). In general, the results are very similar to those obtained at a Reynolds number of one from a qualitative point of view. However, it can be seen from the figures that, for Reynolds number one, the streamlines near the center of the channel seem to curve around the tip of the splitter plate to a greater extent than for Reynolds number ten. This is especially evident for the one-to-nine velocity ratio condition. For example, the streamline originating at (-100, 100) μm tends to diverge laterally around the end of the splitter plate a bit more for the Reynolds number one condition. Although the differences are not large, they are consistent for each flow ratio. Outside of these differences, however, the flow is very similar between the two Reynolds numbers.

Figure 5.22 shows the velocity contour maps of the flow at Reynolds number ten. Comparison to Figure 5.11 leads to the conclusion that the gross flow characteristics between the two Reynolds numbers are more similar than different. As in the Reynolds number one case, as the faster flow passes the splitter plate and expands, the fluid decelerates on the side nearer to the slow moving fluid. This is shown by the asymmetric expansion of the yellow and red regions further downstream in the one-to-five and one-to-nine ratios. Also, note the presence of the short (with respect to downstream distance) region of slower moving fluid just downstream of the splitter plate along the centerline in he one-to-one ratio condition. This is consistent with what was seen in the

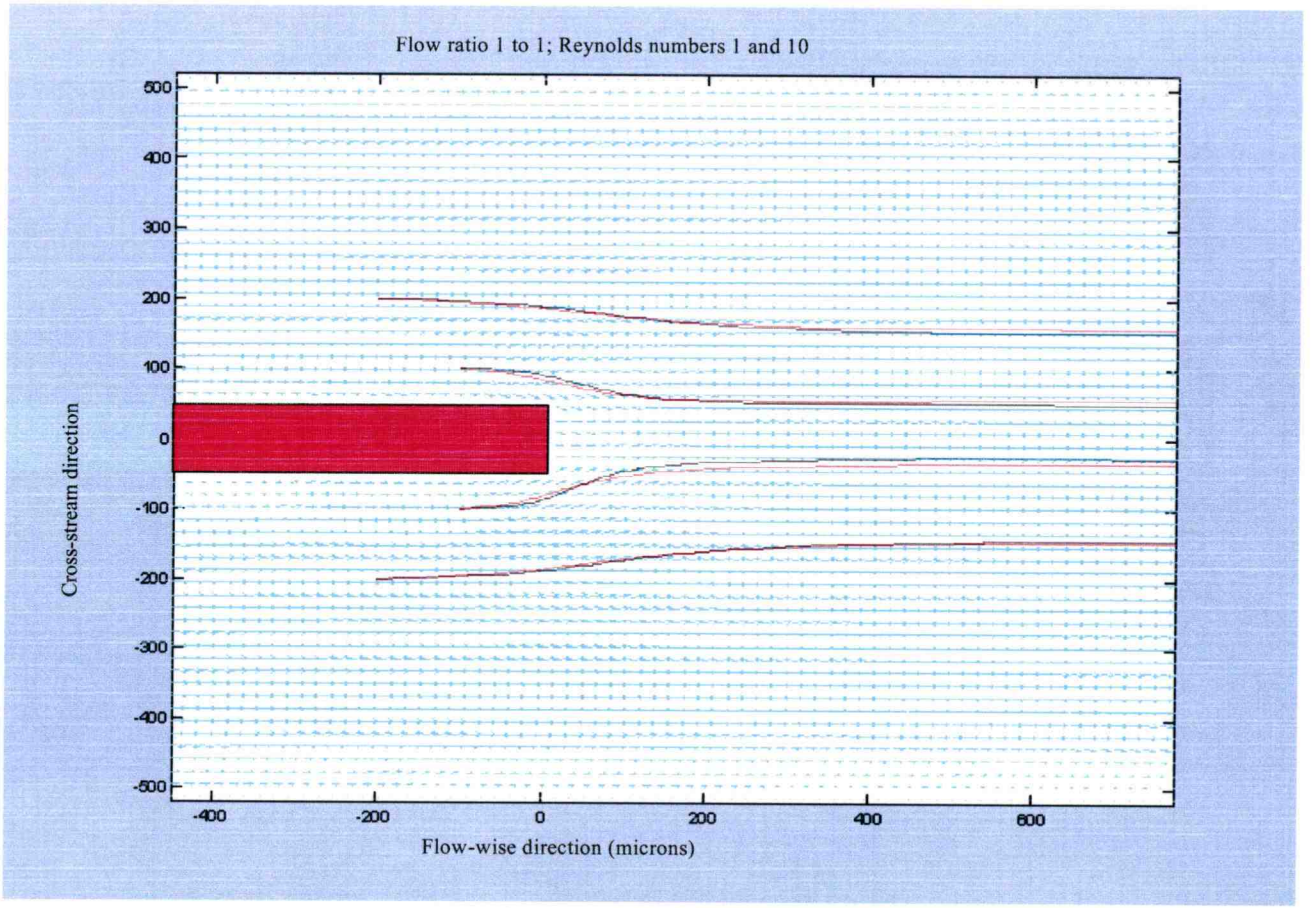

Figure 5.19
Overlay of Reynolds number = 1 and 10 PIV data, Flow ratio one-to-one. The Re=1 streamlines are in black. The Re=10 streamlines are in red. The streamlines originate from (-200, 200), (-200, -200), (-100, 100), and (-100, -100), all in microns.

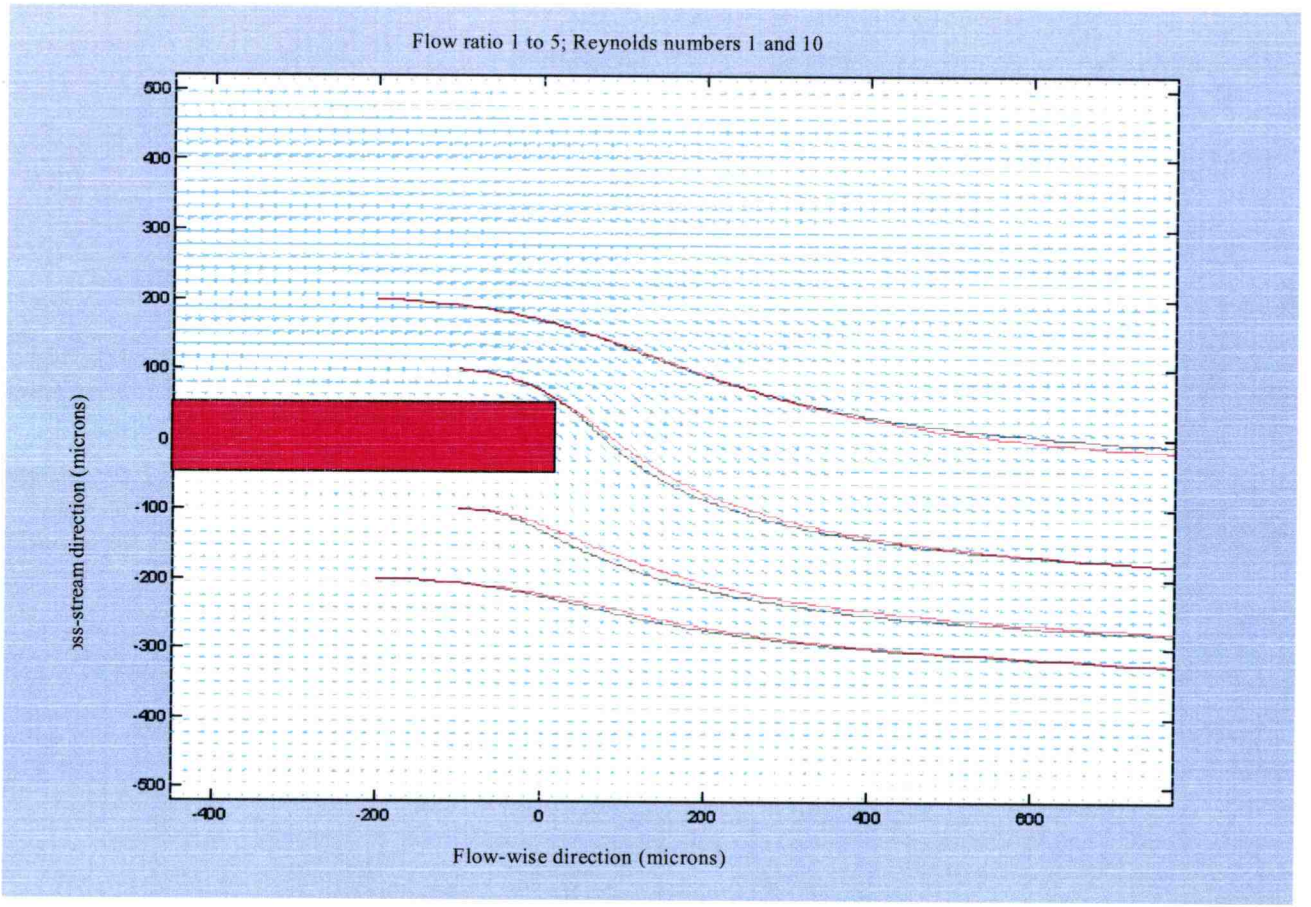

Figure 5.20
Overlay of Reynolds number = 1 and 10 PIV data, Flow ratio one-to-five. The Reynolds = 1 streamlines are in black. The Reynolds = 10 streamlines are in red. The streamlines originate from (-200, 200), (-200, -200), (-100, 100), and (-100, -100), all in microns.

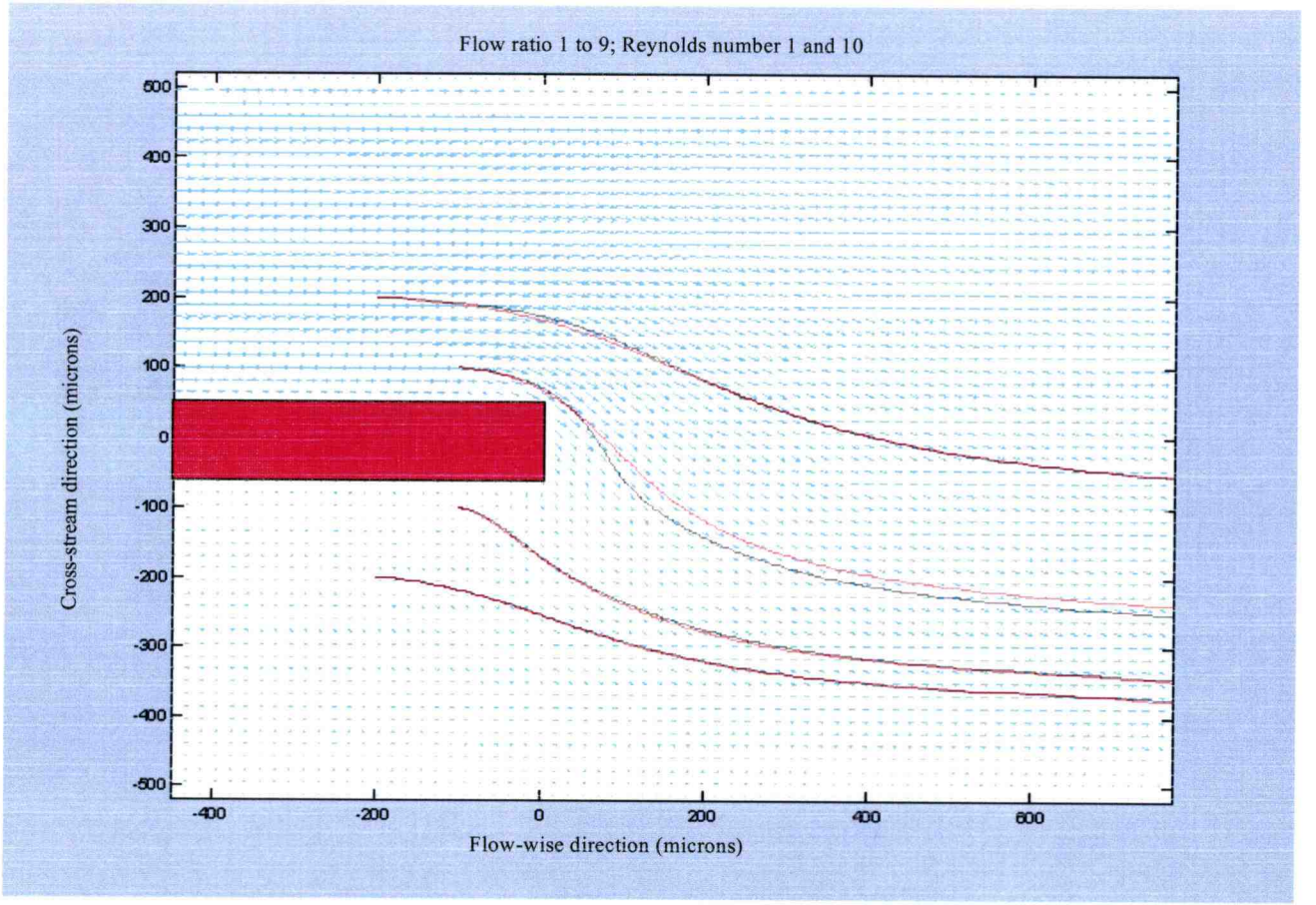

Figure 5.21
Overlay of Reynolds number = 1 and 10 PIV data-Flow ratio one-to-nine. The Reynolds = 1 streamlines are in black. The Reynolds = 10 streamlines are in red. The streamlines originate from (-200, 200), (-200, -200), (-100, 100), and (-100, -100), all in microns

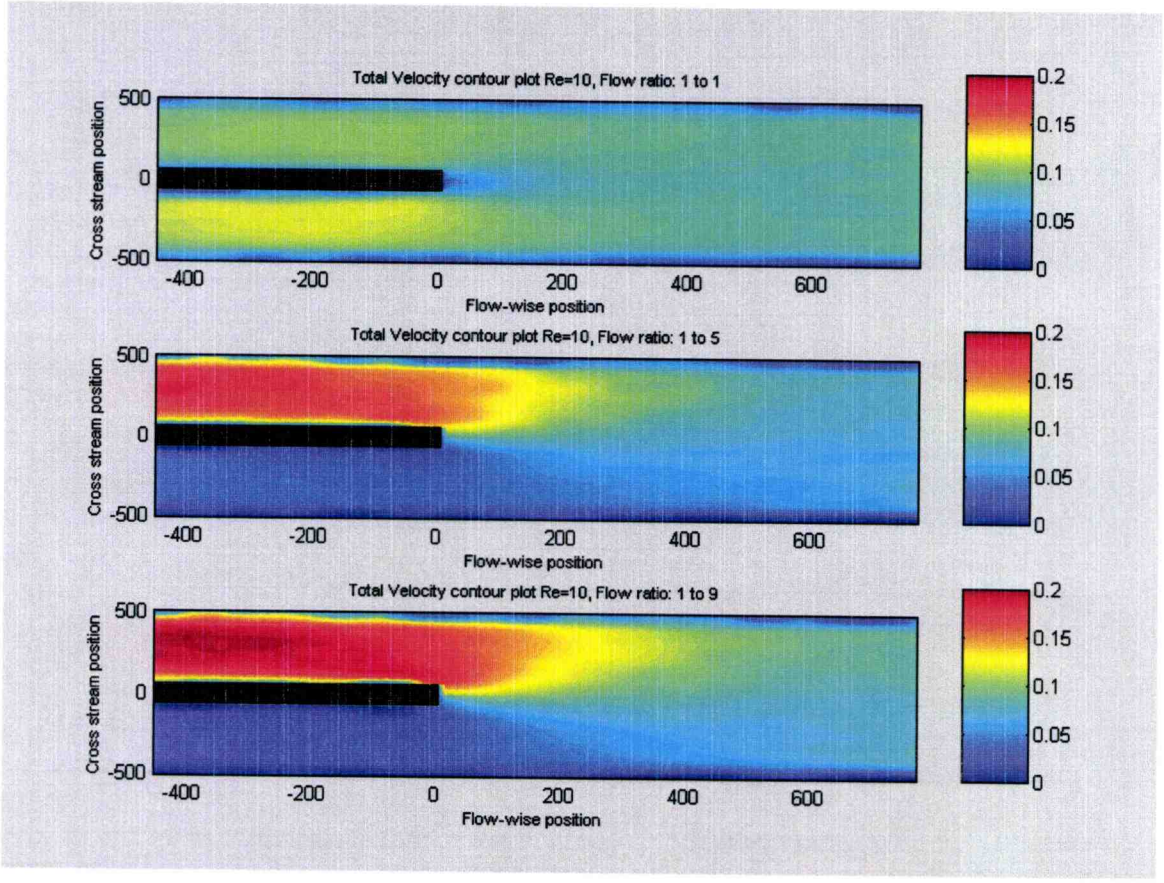

Figure 5.22
Total velocity contour plot, Reynolds = 10. (a) Flow ratio one-to-one, (b) one-to-five, and (c) one-to-nine.

Reynolds number one case (Figure 5.11). Again, the stream-wise velocity profiles in Figure 5.23 demonstrate this shearing phenomenon occurring between the two fluid streams. As with the stream-wise velocity profiles for Reynolds number one, immediately after the end of the splitter plate, the local minimum in velocity that occurs between the fast and slow streams tends to move outward from the center until the flow becomes fully developed across the entire channel.

The cross-stream component of velocity in the Reynolds number ten case (Figure 5.24) also shows a maximum immediately after the splitter plate, indicating a shift from stream-wise momentum flow to lateral momentum flow. However, unlike in the Reynolds number one case, the geometric center of the maximum cross-stream velocity does not seem to shift downstream as the velocity ratios increase (Figure 5.25).

Flow development length

As discussed in the earlier section, once the flow has passed the end of the splitter plate, it undergoes a flow readjustment and then tends to regain flow symmetry as the flow progresses down towards the outlet. The shape of the velocity profile begins to approximate the fully developed velocity profile as described earlier. Given the symmetry of a fully developed velocity profile in internal duct flow, fully developed flow was achieved when the flow rate in the upper half of the channel was equal to the bottom half. Given a certain depth, this is equivalent to the integration of the velocity profile in half of the channel. Therefore, fully developed flow is achieved at the position "x", where:

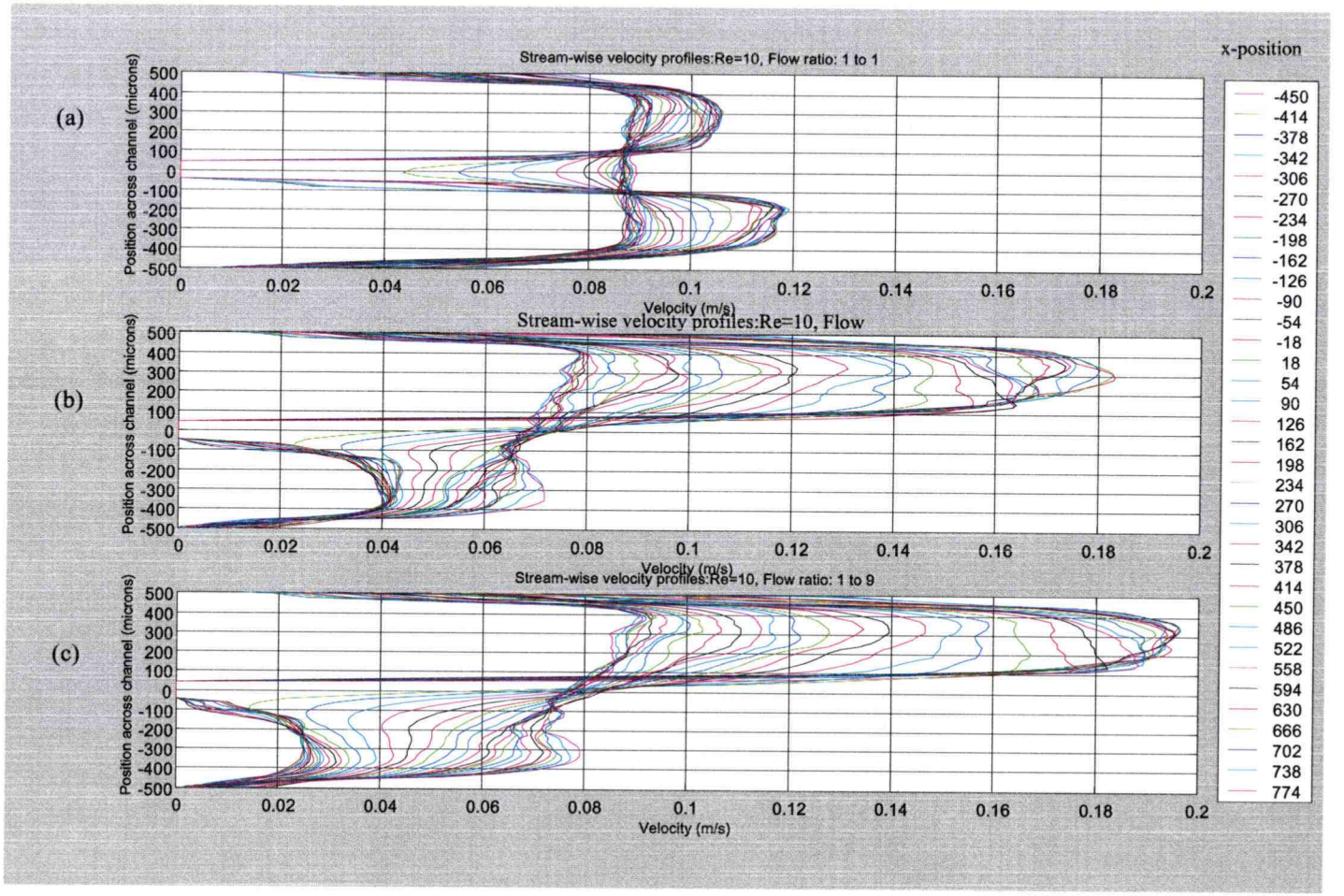

Figure 5.23
Stream-wise velocity profiles- various flow rates, Reynolds = 10. Each line represents a different position downstream along the channel. (a) Flow rate one-to-one, (b) one-to-five, (c) one-to-nine.

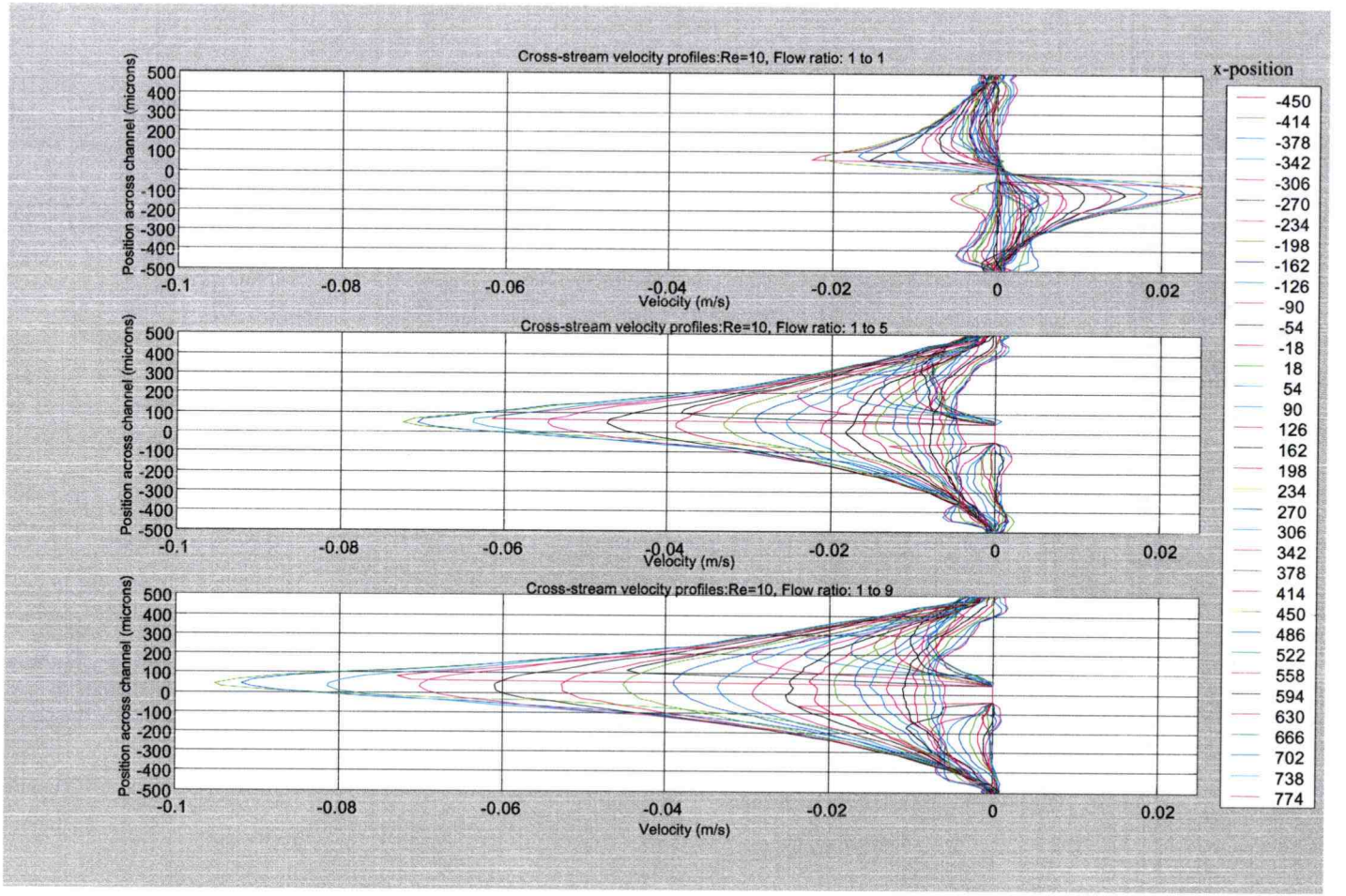

Figure 5.24
Cross-stream velocity profiles- various flow rates, Reynolds = 10. Each line represents a different position along the channel. Flow rates (a) one-to-one, (b) one-to-five, (c) one-to-nine. A negative velocity indicates flow away from the faster stream towards the slower one.

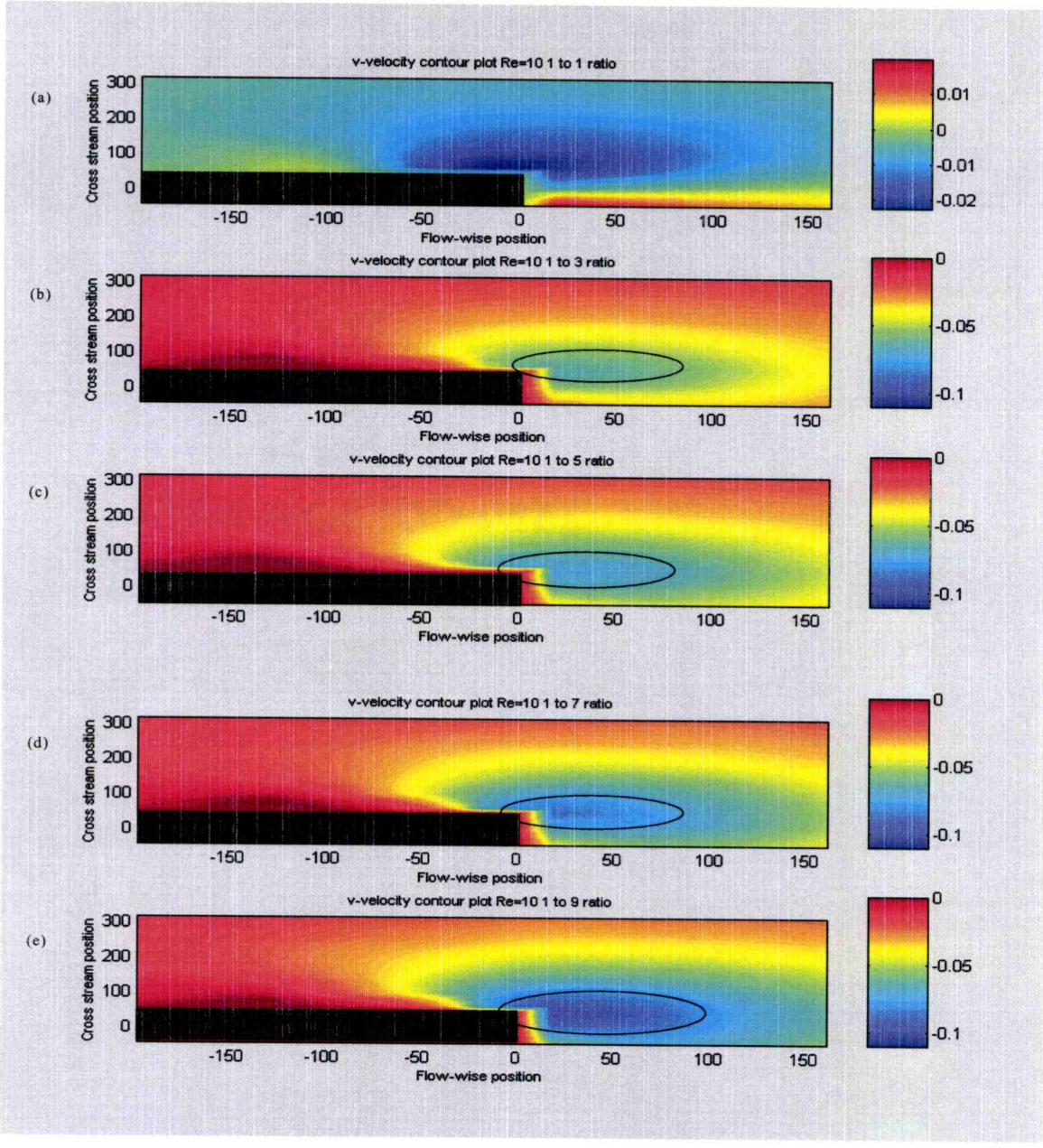

Figure 5.25
Cross-stream velocity contour plot, Reynolds = 10 (zoomed in). Flow ratios (a) one-to-one, (b) one-to-three, (c) one-to-five, (d) one-to-seven, (e) one-to-nine. Note that the elliptical regions do not tend to shift downstream as in the Reynolds = 1 case.

$$Q' = \left(\frac{Q}{\Delta z}\right)_{top} = \int_{0}^{+\frac{w}{2}} velocity_x dy = \left(\frac{Q}{\Delta z}\right)_{bottom} = \int_{0}^{-\frac{w}{2}} velocity_x dy, \qquad (5.10)$$

where Δz is the depth of field. Therefore, the integration for each half of the channel was performed in Figure 5.26. As the plots show, the flow rates in each of the pre-merged channels remains fairly constant before the end of the splitter plate. After the splitter plate, the flow rates begin to converge. Unfortunately, due to limitations in the optical system's field of view, the downstream position at which the curves actually meet (i.e. fully developed flow) was not recorded. However, in order to make a qualitative comparison of the development length for different flow ratios and Reynolds numbers, a modified development criterion was used. Based on the largest difference in Q' between the two streams for the various flow ratios, the flow was considered fully developed when Q' for each channel half was within 8.3% based on the total Q' for the two channels. This situation corresponded to the one-to-nine flow condition. The result for both Reynolds numbers is shown in Figure 5.27. For the one-to-one flow ratio case, the Q' of each channel half remains within the 8.3% fully developed criterion from the outset, immediately after the splitter plate. However, the downstream distance for developed flow increases noticeably, as the flow ratio is increase to one-to-five. After this ratio, however, the development length seems to plateau and become insensitive to the flow ratio. Oak *et al.* (2001) examined the flow development length for a channel of similar geometry, but slightly different dimensions, using a 3-dimensional numerical model. Similar to these results, they also found that, at higher flow rate ratios, the development length was less sensitive to increasing flow ratios

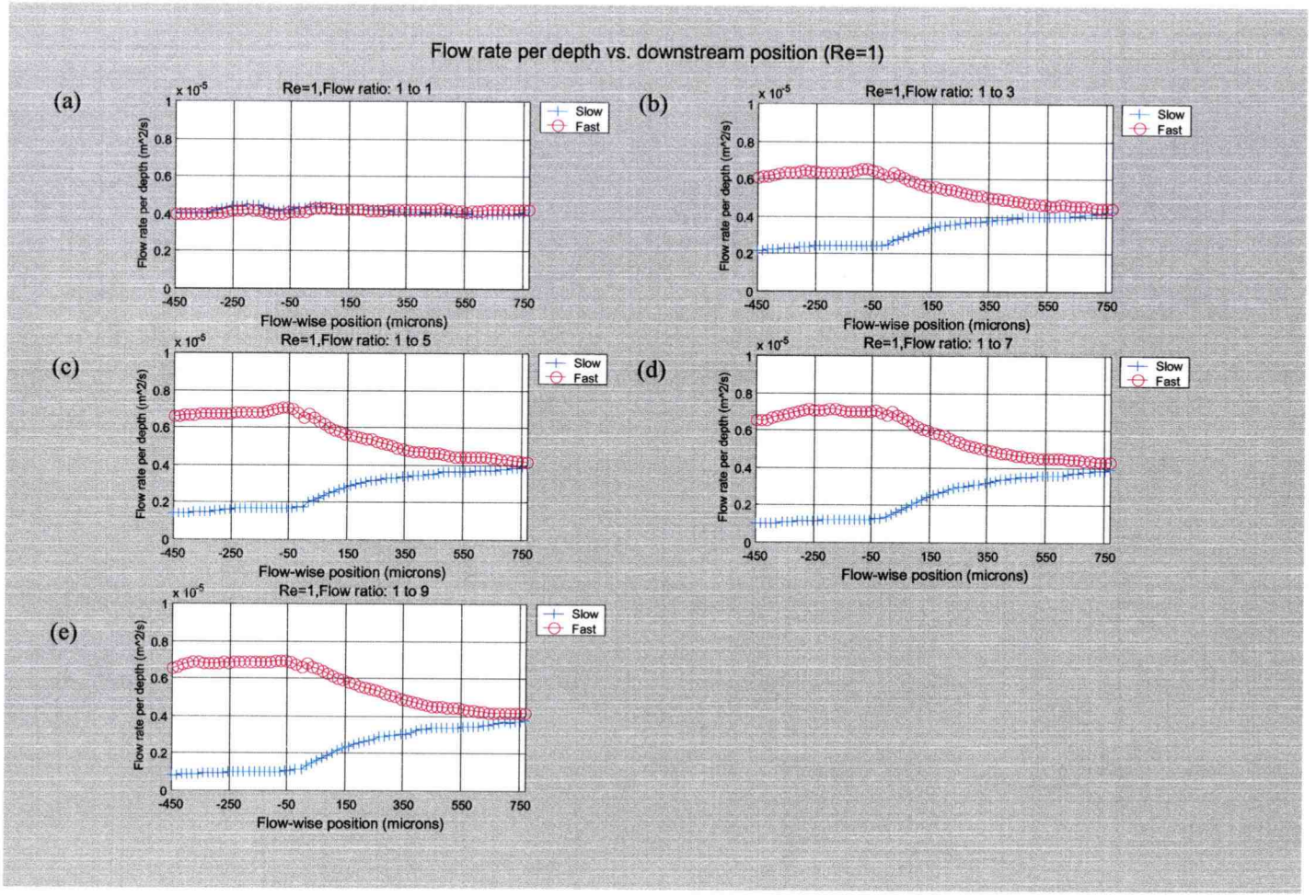

Figure 5.26
Integration of velocity profiles in top (fast) and bottom (slow) halves of channel. Flow ratios: (a) one-to-one, (b) one-to-three, (c) one-to-five, (d) one-to-seven, (e) one-to-nine. All plots are for Reynolds number = 1.

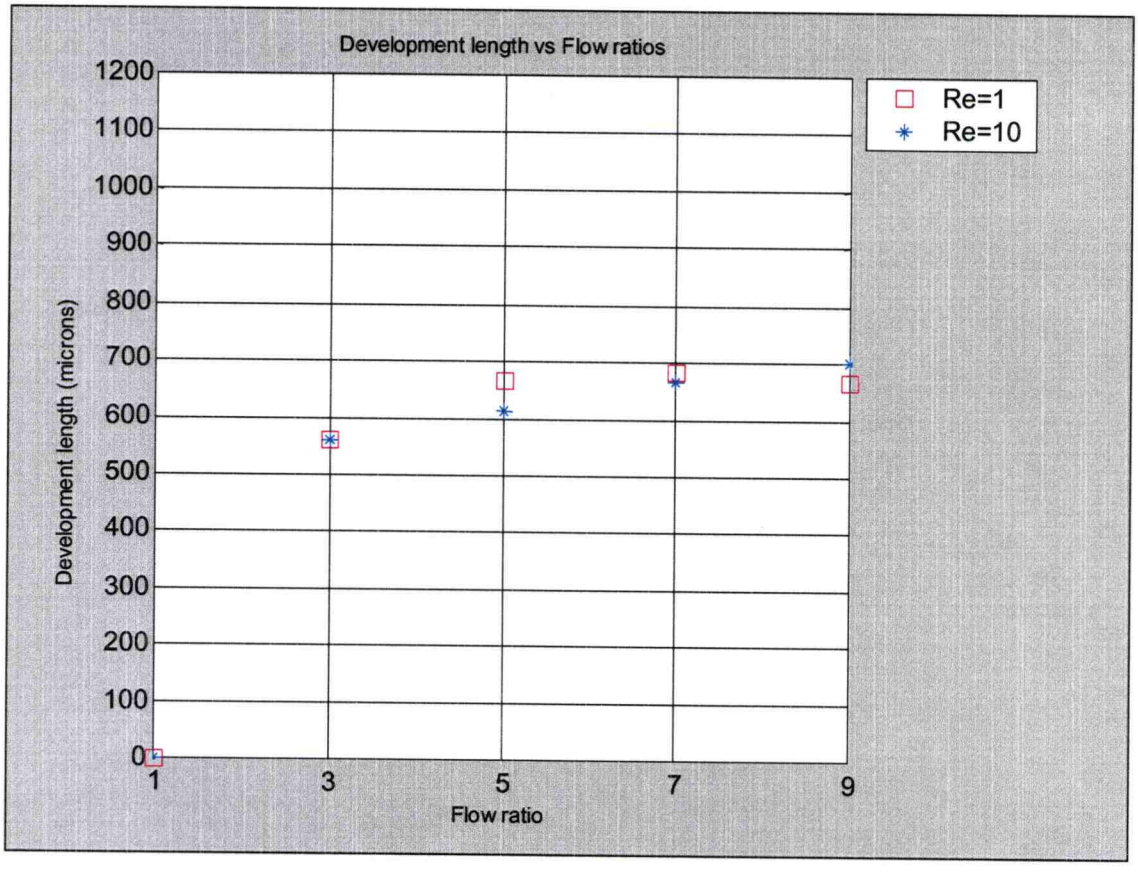

Figure 5.27
Flow development length vs. flow rates for Reynolds = 1 and 10.

Although they are not the same phenomenon, it is interesting to compare the flow development length of parallel streams and the hydrodynamic entry length in a rectangular channel. For laminar flow in a rectangular channel of aspect ratio 16, Shah and London (1978) present an expression for entry length (L_{entry}) as:

$$L_{entry} = D_{hyd}(0.01675 \cdot Re), \tag{5.11}$$

where D_{hyd} is the hydraulic diameter and Re is the Reynolds number based on hydraulic diameter. From this expression, the entry length for a flow with Reynolds number one in a channel of comparable aspect ratio would be approximately 2 μm. In another study, Dombrowski *et al.* (1993) developed a numerical model to study the development length in a circular pipe at low Reynolds numbers. Using these results, the relationship they developed is:

$$L_{entry} = D_{hyd}(0.379\exp(-0.148Re) + 0.0550Re + 0.260). \tag{5.12}$$

Using this relationship, the predicted entry length for a channel similar to the one utilized in this study would be approximately 76 μm. However, according to the data gathered in the present study, the length for flow development in co-flowing stream is an order of magnitude larger than the entry length for a channel of similar Reynolds number and aspect ratio. Therefore, it seems that the length for flow development in merging parallel streams cannot be adequately predicted by current hydrodynamic entry length relationships.

CHAPTER VI

CONCLUSIONS AND RECOMMENDATIONS

This study applied fluorescent dye and PIV visualization techniques to investigate the flow characteristics when two co-flowing laminar fluid streams merge in a rectangular microchannel. By varying the velocity ratios between the two streams as well as varying the main chamber Reynolds number, the interaction of the two streams was found to be ultimately guided by the momentum redistribution between the two streams as they leave the confines of their individual channels and merge together.

The portion of the experiment utilizing the fluorescent dye illustrated the lack of mixing that occurs in this type of low Reynolds number microscale environment. At high velocity ratios, a large lateral momentum transfer was observed with the faster moving fluid rapidly expanding towards the slower fluid, resulting in a compression of the slower moving fluid. However, even at these high velocity ratios and high shear gradients, the mixing between the faster moving fluorescent dye and the slower moving water was shown to be minimal. Additionally, as the fluids continued to progress towards the end of the channel, they remained separate with no apparent diffusional broadening.

The PIV portion of this investigation largely confirmed the speculation of the fluorescent dye studies. From the velocity vector field plots, the expansion of the faster moving fluid around the tip of the splitter plate into the slower moving stream was visually confirmed. It was found that, as the fluid moved around the splitter plate, the magnitude of its velocity actually decreased. However, by decomposing the velocity into cross-stream and flow-wise components, it was found that this was the location of the

maximum cross-stream velocity. As the downstream velocity decreased, the flow-wise momentum was essentially transformed into a lateral velocity. A weak effect of increasing the flow ratio number was the downstream shifting of the center of the maximum cross-stream velocity magnitude. However, this was not seen at the higher Reynolds number flows. As the flow continued downstream, the accelerating local stream-wise velocity minimum between the two streams tended to shift away from the faster stream towards the slower one as the flow progressed downstream. This was described as a wave-like propagation motion resulting from the local shear due to the velocity gradients between the streams.

As the velocity ratios increased, the extent to which the flow diverged around the splitter plate also increased. However, through the use of streamlines, a very slight weakening in this behavior was observed at the higher Reynolds number. With the aforementioned exceptions, the effect of Reynolds number on the characterization of the flow was nominal. The overall qualitative characteristics of the flow were very similar between Reynolds number one and ten. In an attempt to gain insight into the development length of the merging flows, it was found that, beyond a velocity ratio of one-to-three, it is not a strong function of velocity ratio nor does is seem to be dependent on the Reynolds numbers examined in this study. For ratios greater than unity, the flow tends to regain its fully developed nature between four to six hydraulic diameters downstream of the splitter plate. It must be noted that, due to limitations in the range of data collected, an arbitrary criterion for fully developed was applied. Nonetheless, it is believed that the general trend is still valid.

In order to improve upon the results of this experiment, it would be useful to examine the velocity fields further downstream in order to obtain a more quantitative representation of the true development length. Another recommendation would be to increase the range of either Reynolds numbers or velocity ratios. This would be useful in determining the existence of an optimum flow ratio and Reynolds number combination to obtain the maximum cross-stream velocity magnitude. Additionally, it would be beneficial to employ other fabrication techniques such as diffusion soldering, solvent welding, or etching to create a channel with more consistent dimensions. It would also be interesting to utilize a dye or tracer with a diffusion coefficient greater than that of Rhodamine 6G Chloride in order to see more differentiation in the diffusion layer at the interface of the two fluids. A final recommendation would be to design an optical system with the capability of selectively zooming in on particular areas of interest, especially in the region below the splitter plate in the slower stream. It would be of interest to determine the true nature of the flow in the slow fluid near the splitter plate to discover if a re-circulation is present. Due to the interest in imaging the entire flow field, high spatial resolution in critical areas was not achieved in the present study.

BIBLIOGRAPHY

Brody, J.P., Yager, P., Goldstein, R.E., and Austin, R.H., 1996, "Biotechnology at Low Reynolds Numbers", *Biophysical Journal*, Vol. 71, pp. 3430-3441.

Cummings, E.B., 1999, "PIV Measurement of Electro-Osmotic and Pressure-Driven Flow Components in Microfluidic Systems", *MEMS-Vol.1,Microelectromechanical Systems,* ASME, pp. 377-384.

Dombrowski, N, Foumeny, E.A., Ookawara, S., Riza, A., 2001, "Influence of Reynolds number on the entry length and pressure drop for laminar pipe flow", *Canadian Journal of Chemical Engineering*, Vol. 71, no. 3, pp. 472-476.

Fuh, C.B., 2000, "Split-flow Thin Fractionation" *Analytical Chemistry*, A-271 A, pp. 266

Fuh, C.B., Trujillo, E.M, and Giddings, J.C., 1995, "Hydrodynamic Characterization of SPLITT Fractionation Cells", *Separation Science and Technology*, Vol. 30 (20), pp. 3861-3876.

Gosch, M., Blom, H., Holm, J., Heino, T., Rigler, R., 2000, "Hydrodynamic Flow Profiling in Microchannel Structures by Single Molecule Fluorescence Correlation Spectroscopy", *Analytical Chemistry*, Vol. 72, pp. 3260-3265.

Holmes, D.B., and Vermeulen, J.R., 1968, "Velocity profiles in ducts with rectangular cross sections", *Chemical Engineering Science,* Vol. 23, pp. 717-722.

Incropera, F.P., and DeWitt, D.P., 1996, "Fundamentals of Heat and Mass Transfer," 4th Edition, New York : Wiley.

Ismagilov, R.F., Stroock, A.D., Kenis, P.J.A., Whitesides, G., 2000, "Experimental and theoretical scaling laws for transverse diffusive broadening in two-phase laminar flows in microchannels", *Applied Physics Letters*, Vol. 76, No. 17, pp. 2376-2378.

Kenis, P.J.A., Ismagilov, R.F., Whitesides, G.M., 1999, "Microfabrication Inside Capillaries Using Multiphase Laminar Flow Patterning", *Science*, Vol. 285, pp. 83-85.

Kenis, P.J.A., Ismagilov, R.F., Takayama, S, Whitesides, G.M., Li, S., White, H.S., 2000, "Fabrication inside Microchannels Using Fluid Flow", *Accounts of Chemical Research*, Vol. 33, pp. 841-847.

Ligrani, P.M., Gupta, S., Giddings, J.C., 1998, "Onset and effects of instabilities from unstable stratification of density on mass transfer in channel shear layers at low Reynolds numbers", *International Journal of Heat and Mass Transfer*, Vol. 41, No. 12, pp. 1667-1679.

Meinhart, C.D., Wereley, S.T., Santiago, J.G., 1999, "PIV Measurements of a Microchannel Flow", *Experiments in Fluids*, Vol. 27, pp. 414-419.

Oak, J., Pence, D.V., Liburdy, J.A., 2001, "Diffusion and Flow Development in Co-Flowing Micro-Channel Streams", Accepted for publication in *Microscale Thermophysical Engineering*

Santiago, J.G., Wereley, S.T., Meinhart, C.D., Beebe, D.J., Adrian, R.J., 1998, "A particle image velocimetry system for microfluidics", *Experiments in Fluids*, Vol. 25, pp.316-319.

Wereley, S.T., Meinhart, C.D., Santiago, J.G., Adrian, R.J., 1998, "Velocimetry for MEMS Applications", American Society of Mechanical Engineers, Dynamic Systems and Control Division (Publication) DSC v 66 Nov 15-20, pp. 453-459

APPENDIX

APPENDIX

UNCERTAINTY ANALYSIS

The purpose of this appendix is to present the uncertainty of the velocity measurements and the Reynolds number.

Velocity (PIV)

In the PIV portion of the study, the velocity vectors were calculated by measuring the displacement between particles in two separate video images within a short time interval. The formula for velocity is:

$$v = \frac{\Delta s}{\Delta t}, \tag{A.1}$$

where Δs is the displacement of a particle and Δt is the time interval between successive images. The uncertainty in the velocity is estimated using the Kline-McClintock relationship:

$$u_v = \sqrt{\left(\frac{\partial v}{\partial \Delta s} u_{\Delta s}\right)^2 + \left(\frac{\partial v}{\partial \Delta t} u_{\Delta t}\right)^2}, \tag{A.2}$$

where u_v, $u_{\Delta s}$, and $u_{\Delta t}$ are the uncertainties in velocity, displacement, and time, respectively.

Time uncertainty

From the manufacturer specification, the uncertainty associated with the delay generator is given as:

$$u_{\Delta t} = 1.5 \text{ ns} + \text{Timebase error x } \Delta t \qquad \text{(A.3)}$$

For the timebase utilized in the current study, the error is given as < 25 ppm. Therefore, for Reynolds number one, (Δt = 400μs), $u_{\Delta t}$ is approximately 11.5 ns. Similarly, for Reynolds number ten, (Δt = 40 μs), $u_{\Delta t}$ is approximately 2.5 ns.

Displacement uncertainty

The uncertainty in the displacement has a bias ($B_{\Delta s}$) and a precision ($P_{\Delta s}$) component:

$$u_{\Delta s} = \sqrt{(B_{\Delta s})^2 + (P_{\Delta s})^2} \qquad \text{(A.4)}$$

The bias component is a consequence the optical setup and the software processing systems. In PIV analysis at small scales, the effective diameter of the particle fluorescence projected back onto the flow field is what limits the spatial resolution. (Wereley *et al.,* 1998). The characteristic diameter of the point spread function is given by Wereley *et al.* (1998) as:

$$d_s = 2.44M\frac{\lambda}{2NA} \qquad \text{(A.5)}$$

where M is the total system magnification, λ is the wavelength of the recording light, and NA is the numerical aperture of the objective. In the current setup, the point spread function, d_s, is 12444. Since the recorded image is a "convolution of the geometric image with the diffraction-limited image," by using a Gaussian approximation, the effective particle diameter is given as (Wereley *et al.,* 1998):

$$d_e = \left[M^2 d_p^2 + d_s^2\right]^{1/2} \qquad \text{(A.6)}$$

Therefore, for this setup, the effective particle image diameter on the CCD array, d_e, becomes 12.44 μm. Therefore, given a system magnification of 5, the effective particle diameter superimposed on the flow is 2.5 μm. According to Wereley *et al.* (1998), Given that a particle diameter is resolved by 3-4 CCD pixels, the location of the correlation peak can be located to with one-tenth of the effective diameter. Therefore, a bias uncertainty for the position of the particle in the flow can be estimated as:

$$P_{\Delta s} = \frac{d_e}{10M} \tag{A.7}$$

Using this expression, the bias uncertainty in the displacement in the current PIV setup is estimated be estimated as 0.25 μm.

There is also a precision uncertainty associated with the displacement. The VISIFLOW software calculates velocities using a time separation input by the user. Therefore, a displacement field can be extracted from the velocity data without the need to incorporate any uncertainty in time. In addition, because the velocity field (and, hence, displacement field) presented for each velocity ratio is actually an average of several velocity fields, a precision uncertainty in the displacement can be found from:

$$P_{u\Delta s} = \frac{S_{\Delta s}}{N^{\frac{1}{2}}}, \tag{A.8}$$

where $S_{\Delta s}$ is the standard deviation of the displacement and N is the number of fields in the sample.

Using these relationships, the average uncertainties were found to be approximately 0.0007 m/s for the Reynolds one case and 0.0065 m/s for the Reynolds ten case. Tables A.1 and A.2 show the absolute and relative uncertainties, respectively, in more detail. It should be noted that the high maximum uncertainties were found in the

regions of slower moving fluid, either near the walls of the channel or next to the splitter plate. In addition, they are not representative of the uncertainties involved in majority of the flow field.

Table A.1 Absolute uncertainties for velocity

Flow condition	Minimum Uncertainty (m/s)	Maximum Uncertainty (m/s)	Average Uncertainty (m/s)	Standard Deviation
Reynolds=1, 1:1 ratio	0.0006	0.0018	0.0007	0.00010
Reynolds=1, 1:3 ratio	0.0006	0.0009	0.0007	0.000025
Reynolds=1, 1:5 ratio	0.0006	0.0016	0.0009	0.00020
Reynolds=1, 1:7 ratio	0.0006	0.0014	0.0007	0.000063
Reynolds=1, 1:9 ratio	0.0006	0.0012	0.0007	0.000064
Reynolds=10, 1:1 ratio	0.0063	0.009	0.0064	0.00021
Reynolds=10, 1:3 ratio	0.0063	0.0123	0.0065	0.00033
Reynolds=10, 1:5 ratio	0.0063	0.014	0.0065	0.00041
Reynolds=10, 1:7 ratio	0.0063	0.013	0.0065	0.00044
Reynolds=10, 1:9 ratio	0.0063	0.015	0.0065	0.00045

Table A.2 Relative uncertainties for velocity

Flow condition	Minimum Uncertainty (%)	Maximum Uncertainty (%)	Average Uncertainty (%)	Standard Deviation
Reynolds=1, 1:1 ratio	5.2	70.8	8.6	5.6
Reynolds=1, 1:3 ratio	3.6	43.4	8.6	4.4
Reynolds=1, 1:5 ratio	4.8	40.5	10.4	4.4
Reynolds=1, 1:7 ratio	3.3	112	10.9	9.1
Reynolds=1, 1:9 ratio	3.3	133.8	11.5	9.8
Reynolds=10, 1:1 ratio	5.3	34.4	7.4	2.1
Reynolds=10, 1:3 ratio	3.6	90.6	10.3	6.2
Reynolds=10, 1:5 ratio	3.3	65.8	11.3	6.6
Reynolds=10, 1:7 ratio	3.2	93.4	12.2	8.7
Reynolds=10, 1:9 ratio	2.9	122.2	12.8	11

Reynolds number

The Reynolds number (Re) is given by the following relationship:

$$\mathrm{Re} = \frac{\left(\frac{Q}{A}\right) d_h}{\nu}, \qquad \text{(A.9)}$$

where Q is the volumetric flow rate, A is the cross-sectional area, d_h is the hydraulic diameter of the channel, and ν is the kinematic viscosity of the fluid. The uncertainty for the Reynolds number is estimated using the Kline-McClintock relationship:

$$u_{Re} = \sqrt{\left(\frac{\partial \mathrm{Re}}{\partial Q} u_Q\right)^2 + \left(\frac{\partial \mathrm{Re}}{\partial A} u_A\right)^2 + \left(\frac{\partial \mathrm{Re}}{\partial d_h}\right)^2 + \left(\frac{\partial \mathrm{Re}}{\partial \nu} u_\nu\right)^2}. \qquad \text{(A.10)}$$

From the manufacturer specifications for the syringe pumps, the uncertainty in the flow rate, Q, was 0.17 μl/min and 1.7 μl/min for the Reynolds number one and ten conditions, respectively. The microscopes used to measure A and d_h introduced an uncertainty of u_A = 3020 μm^2 and u_{d_h} = 5.7 μm. Assuming a temperature variation of ±5°C, the variation in the kinematic viscosity is approximately 10% at one atmosphere. Therefore, the uncertainty in the Reynolds number is approximately 12%.